Interfacial engineering of $Bi_{12}O_{17}Br_2$/g-C_3N_{4-x} S-scheme junction boosting charge transfer for cooperative tetracycline decomposition and CO_2 reduction

Xuemei Jia, Jing Cao [*], Haoyu Sun, Xinyue Li, Haili Lin, Shifu Chen [*]

College of Chemistry and Materials Science, Key Laboratory of Green and Precise Synthetic Chemistry and Applications, Ministry of Education, Huaibei Normal University, Huaibei, Anhui 235000, PR China

A B S T R A C T

To realize the double winning goal of environment and energy, a novel dual-functional photocatalytic reaction system is designed by using CO_2 conversion and pollutant oxidation in one cooperative system. S-scheme heterojunctions exhibit huge potential for accomplishing such synergetic coupling reaction system due to their strong redox ability and speedy charge separation rate. Howbeit, how to effectively adjust the charge transfer rate at nanometric heterointerface remains pivotal and challenging. Herein, interfacial Bi-N bond and N vacancy co-modulate $Bi_{12}O_{17}Br_2$/g-C_3N_{4-x} S-scheme junction is constructed, which not only presents superior separation and migration efficiency of charges, but also possesses high redox capacity. A series of theoretical and experimental results manifest that the synergistic effect of interfacial Bi-N bond and N vacancy availably expedite carrier transfer dynamics, achieving excellent photo-redox activity for cooperative CO_2 reduction and tetracycline oxidization. Furthermore, compared to two half-reactions, such elaborate cooperative reaction system displays an obviously elevated photo-redox activity. This work provides a deep insight into regulating interfacial charge migration of heterojunction by chemical bonds and defects.

1. Introduction

Environmental contamination and energy shortage have made a great deal of negative influences for human livelihood. Thus, it is extremely desirable to inquire cost-effective technology for environmental remediation and energy generation without secondary pollution [1–3]. Lately, photocatalysis technology is a potential and attractive approach to purify the environment and generate solar fuel, such as toxic pollutants decomposition [4–6], CO_2 reduction into fuels [7–9], water splitting to generate H_2 [10–13] under solar light irradiation. In particular, the photocatalytic CO_2 reduction could not only produce solar fuels, but also relieve the greenhouse effect, which has been considered as an effective tactic to deal with the existing environmental and energy problems. At present, most researchers commonly focus on the reductive half-reaction of CO_2 photoreduction, but the oxidative half-reaction is often overlooked [14–16]. Although the emerging photo-redox coupling of organics oxidation synthesis with CO_2 reduction has been deemed as an appealing solution to resolve the above-mentioned issues [17–19], it could likely cause secondary

pollution due to the generated by-products and residual organic solvents. Therefore, it is primary task to reasonably design an ideal photo-redox coupling system for simultaneously addressing energy and environmental issues. Starting from the reverse of oxidative half-reaction of aforementioned coupling reaction system, an ideal coupling reaction system for CO_2 photoreduction and organic decomposition was constructed by replacing "organic synthesis" with "organic decomposition", which not only the win-win target of energy and environment could come true, but also the photoelectrons and holes could be fully utilized. More importantly, such designed photo-redox coupling of CO_2 reduction with organic decomposition is extremely feasible, which has been confirmed by our previous work [20–22].

Thus, it is very essential to devise highly efficient catalysts with swift transfer rate of carriers, strong redox potential and sufficient active sites for such synergetic coupling reaction system. Graphitic carbonic nitride (g-C_3N_4), as a nonmetallic semiconductor, has emerged as an appealing photocatalyst to mitigate the impending environmental and energy crisis owing to its suitable band gap, strong reducing capacity, good chemical stability and environmentally friendly property [20,23,24].

Howbeit, the limited active sites and poor light absorption have immensely restricted its visible light photocatalytic performance. Recently, the introduced defects could effectually conquer the above inherent weakness. For example, Yu et al. demonstrated that the nitrogen (N) vacancy in g-C_3N_4 not only increased reactive sites, but also extended light absorption [25]. Moreover, Majima's team further found that N vacancy as electron traps could effectively capture electrons of g-C_3N_4 surface, thereby expediting the separation of photogenerated charges [26]. Despite the defects could obviously ameliorate the catalytic performance of pure g-C_3N_4 through capturing photoelectrons, extending light absorption and providing more active sites, it is still quite hard for mono-component N defective g-C_3N_4 (denoted as CNx) to satisfy the needs of the above coupled reaction system in virtue of its inferior oxidation potential and speedy recombination rate of charges, which depended on its inherent band structure.

As is well known, the construction of Z-scheme heterostructures possessed great potential for fulfilling such designed photo-redox catalyzed reaction system on account of the strong redox potential and unique charge transfer pathway [27,28]. Among Z-scheme family, traditional Z-scheme heterojunction with redox couples was confined to the solution phase. Beyond that the electron transfer route of the liquid-phase Z-scheme system was not thermodynamically desirable because photon-generated carriers with greater redox capacity could react more easily with redox pairs [27]. Although all-solid-state Z-scheme heterojunction could be widely used, the swift electron transfer was difficult to achieve due to two Schottky barriers at the metal/semiconductor interface [28]. In contrast, direct Z-scheme heterojunctions, as an ideal system, could effectively avoid the above problems. Nevertheless, there is abundant confusions over direct Z-scheme, because its first and second generations—traditional Z-scheme and all-solid-state Z-scheme—were regarded as premature and problematic [29]. Subsequently, Yu et al. proposed a new concept Step-scheme (S-scheme) heterojunction to replace the usage of "Z-scheme", which was developed according to the advantages of direct Z-scheme heterojunction. Compared with the Z-scheme heterojunction, the S-scheme heterojunction further enhanced the reservation of photogenerated electrons and holes on the conduction band (CB) of the reducing semiconductor and on the valence band (VB) of oxidizing semiconductor, respectively. This is mainly attributed to the band bending of semiconductor and the driving force of the built-in electric field [29]. This charge transfer mode maximized the reservation of photo-generated carriers, which was liable to achieve the excellent photocatalytic redox performance. However, how to adjust and control the charge migration at the interface of S-scheme heterojunction remained a huge challenge.

Newly, the rational design of chemical bond-bridged at the junction interface, such as the C-S bonds in g-C_3N_4/$Bi_{19}Br_3S_{27}$ [30], Bi-O bond in $Bi_2Sn_2O_7$/BiOBr [31], as well as Mo-N bond in MoO_{3-x}/S-CN heterojunction [32], has made great progress to remarkably improve the migration direction of carriers in the S-scheme system. Moreover, defective regions of CNx have affluent delocalized electrons and coordinatively unsaturated atoms, which serve as anchor sites for other semiconductors, forming unique interfacial chemical bonds between CNx and semiconductors. Thus, deliberately establishing CNx-based S-scheme heterojunction with a chemical bond-bridged is expected to be an appealing approach for the construction of highly efficient photocatalysts. Since CNx owned strong reducing ability and negative conduction band potential (E_{CB}), which as a reducing semiconductor would combine with an oxidizing semiconductor to fabricate S-scheme heterojunction. Lately, $Bi_{12}O_{17}Br_2$ [33–35], as a representative Bi-rich bismuth bromide material, has atomic coordination configurations, which can effectively form interfacial chemical bonds with CNx. Beyond that, $Bi_{12}O_{17}Br_2$ with strong oxidizing ability as an oxidative-type semiconductor could establish S-scheme heterojunctions with CNx, which not only obviously expedited the transition rate of interfacial charges, but also maximized redox capacity of photo-excited carriers. So far,

there are very few reports on the establishment of $Bi_{12}O_{17}Br_2$/CNx S-scheme heterojunction with high-quality charge transfer by synchronously defects and interfacial chemical bonds.

Herein, a novel S-scheme $Bi_{12}O_{17}Br_2$ modulated N defective g-C_3N_4 (marked as BOB/CNx) heterojunction with Bi-N bonds was constructed, in which the Bi-N bonds bridge reduced the interface migration resistance, meanwhile, N vacancy provided more reactive sites, thus optimizing the separation efficiency of photogenerated charges. Furthermore, such cooperative photo-redox reaction system displayed high-efficiency photo-redox activity for CO_2 conversion and tetracycline (TC) decomposition in comparison to the corresponding oxidation and reduction half-reactions. This study supplied novel insights into precisely regulating the separation direction of photoinduced carriers for high performance photocatalyst, and further confirmed the underlying application for synergetic CO_2 reduction and pollutants degradation.

2. Experimental

2.1. Synthesis of photocatalysts

First, bulk g-C_3N_4 was synthesized by calcining dicyandiamide at 550 °C (0.5 °C/min) for 2 h in air, which was named as CN. Soon afterwards, the yellow product was ground into powder. In the same way, N defective g-C_3N_4 (marked as CNx) was fabricated by calcining bulk CN powder under N_2 atmosphere.

Next, a range of $Bi_{12}O_{17}Br_2$/CNx photocatalysts were prepared through simplified deposition-precipitation means. Typically, Bi(NO_3)$_3$•5 H_2O (0.485 g) was dispersed into aqueous solution (30 mL) including urea (8 g). Whereafter, CNx (0.97 g) was decentralized evenly in the above solution (solution A). Simultaneously, hexadecyl trimethyl ammonium bromide (0.365 g) was added into deionized water (30 mL) (solution B). In quick succession, solution B was dropped into solution A with sequential agitation. After 1 h, the sediment was rinsed with absolute ethanol and distilled water for six times, and dried at 60 °C for 8 h. The fabricated sample was 25 wt% $Bi_{12}O_{17}Br_2$/CNx (marked as 25BOB/CNx). Similarly, a series of $n$$Bi_{12}O_{17}Br_2$/CN$x$ (n = 5, 15, 35 and 45) heterojunctions with diverse weight ratios were prepared by the same method but altering the dosages of CNx, where n represented the weight percentage of $Bi_{12}O_{17}Br_2$ to CNx. In addition, the synthesis process of $Bi_{12}O_{17}Br_2$/CNx photocatalyst was displayed in Fig. 1a.

Similar to the preparation process of 25BOB/CNx, the 25 wt% $Bi_{12}O_{17}Br_2$/CN without N defect (labeled as 25BOB/CN) was fabricated by replacing CNx with CN.

For comparison, pristine $Bi_{12}O_{17}Br_2$ (named as BOB) was also synthesized according to the preparation of $Bi_{12}O_{17}Br_2$/CNx in the absence of CNx.

2.2. Photocatalytic measurement

Photo-redox integrating of CO_2 conversion with TC decomposition were tested in CO_2 reaction system (MC-SPB10-AG, Beijing Merry-Change Technology Co., Ltd) utilizing a 300 W xenon lamp (MC-PF300C) as illuminant. Briefly, 0.05 g of samples were spread into 50 mL of TC solution via 6 min of ultrasound. Subsequently, the reactor and reaction system were joined together in a vacuum. Whereafter, 99.999% CO_2 as reactant gas, was injected into reaction system. The reaction temperature was continuously kept at 6 °C. The gas product was detected by a Fuli GC9790II gas chromatograph. Ultimately, the liquid was taken out and then centrifuged to obtain the supernatant liquid. At length, the supernatant liquid was measured utilizing a UV–vis spectrophotometer (UV-3600 iplus, Shimadzu).

In addition, the detailed characterization method (Text S1), photoelectrochemical tests (Text S2), density functional theory (DFT) calculations (Text S3), apparent quantum yield (AQY) (Text S4) as well as the calculation of surface charges transfer efficiency (η_{CTE}) (Text S5) were given in Electronic Supporting Information (ESI).
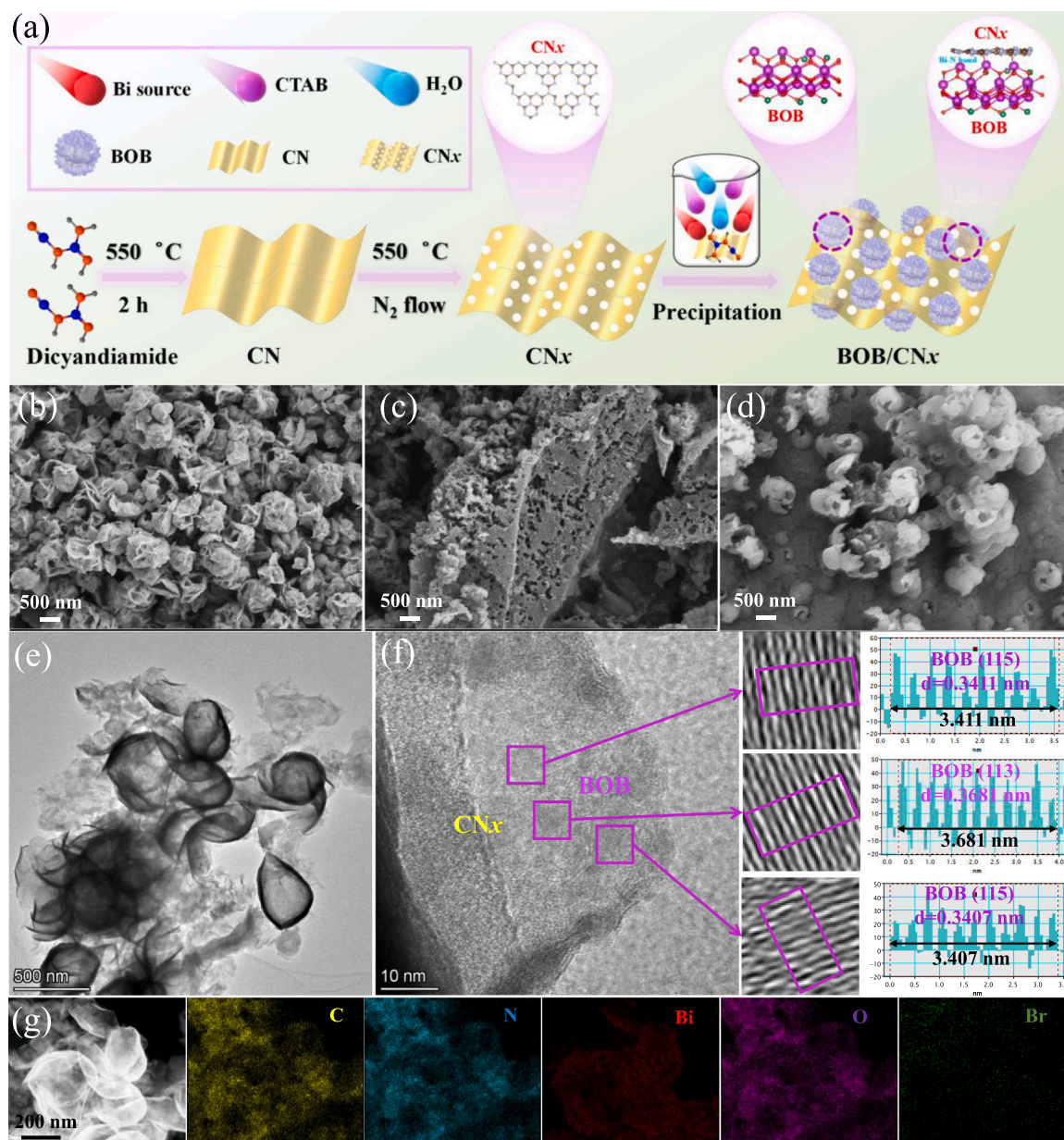
Fig. 1. (a) The preparation procedure of BOB/CN*x*; SEM images of (b) BOB, (c) CN*x* and (d) 25BOB/CN*x*; (e) TEM, (f) HRTEM images and (g) STEM elemental mappings of 25BOB/CN*x* composite.

3. Results and discussion

3.1. Structure analysis

Firstly, the microstructural characters of fabricated samples were monitored through scanning electron microscopy (SEM). As presented in Fig. 1b, single BOB exhibited well-proportioned flower-like structures. Once BOB combined with CN*x* nanosheets (Fig. 1c), it could be discovered that abundant flower-like BOB evenly distributed on the surface of CN*x* nanosheets (Fig. 1d). As observed by transmission electron microscopy (TEM), the flower-like BOB was closely linked to CN nanosheet (Fig. 1e), which was consistent with SEM observation. Furthermore, the corresponding high-resolution TEM (HRTEM) presented intimate interfacial interaction (Fig. 1f), in which not only legible lattice spacing of 0.341 and 0.368 nm identifying to (115) and (113) plane of BOB was discovered, respectively, but also an amorphous CN*x* was also found, confirming the formation of close-knit heterojunction interface between BOB and CN*x*. In addition, the STEM elemental

mappings of 25BOB/CN*x* (Fig. 1g) expressly certified that the elements of Bi, O, Br, C and N uniformly distributed in the 25BOB/CN*x* hybrid, manifesting that BOB was triumphantly anchored on CN*x*.

Whereafter, X-ray diffraction (XRD) was implemented to measure the crystallographic structure of as-synthesized photocatalysts. As exhibited in Fig. 2a, the primary characteristic peak of CN at 26.5° was pertained to (002) plane of g-C_3N_4 (JCPDS No. 87–1526). After introducing N defect, the (002) diffraction faces of CN*x* shifted mildly toward higher angles due to the disappearance of N species from CN skeleton, which was more distinctly observed from the amplifying diffraction region between 25° and 30° (Fig. S1). For pure BOB, all diffraction patterns were consistent with tetragonal $Bi_{12}O_{17}Br_2$ (JCPDS No. 37–0701). When CN*x* coupled with BOB, the diffraction peaks assigning to CN*x* and BOB appeared in all BOB/CN*x* hybrids. Furthermore, the peak intensities of CN*x* gradually reduced while those of BOB increasingly strengthened as the content of BOB increased, reconfirming that the BOB/CN*x* heterojunctions were successfully constructed. For comparison, the diffraction peaks of 25BOB/CN without N defect also
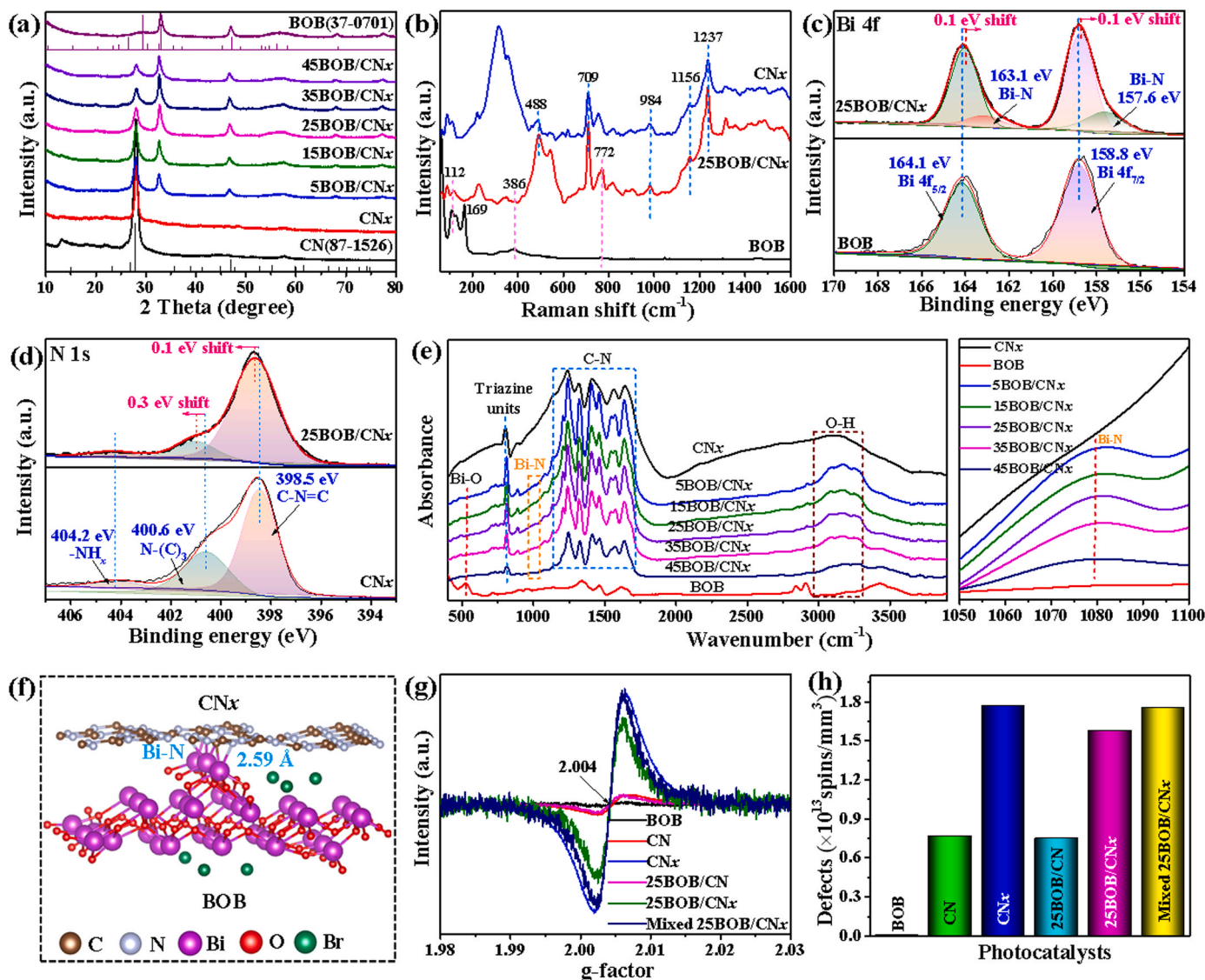
Fig. 2. (a) XRD patterns of BOB, CN*x* and BOB/CN*x* heterojunctions; (b) Raman analysis of BOB, CN*x* and 25BOB/CN*x*; (c) Bi 4 f XPS spectra of BOB and 25BOB/CN*x*; (d) N 1 s XPS spectra of CN*x* and 25BOB/CN*x*; (e) FT-IR spectra of the as-obtained catalysts; (f) Structure model of interfacial Bi-N bond between BOB and CN*x*; (g) EPR spectra and (h) corresponding defect concentrations of the as-prepared samples.

corresponded well to the characteristic peaks of bare CN and BOB (Fig. S2), which manifested the formation of heterojunction. Subsequently, Raman spectroscopy (Fig. 2b) was measured to explore the surface structures of materials. For pure CN*x*, several asymmetric peaks at 488, 709, 984, 1156 and 1237 cm^{-1} were pertained to C–N and C=N heterocycles [36–38]. After introducing BOB, some new characteristic peaks were found at 112, 386 and 772 cm^{-1} for 25BOB/CN*x*, corresponding to Bi-O stretching modes [39], which further confirmed that the as-obtained sample herein was heterojunction.

In quick succession, X-ray photoelectron spectroscopy (XPS) was utilized to explored the interfacial interaction between CN*x* and BOB. The XPS full spectra (Fig. S3a) manifested the existence of N and C elements stemming from CN*x*, as well as Bi, Br, and O elements coming from BOB in 25BOB/CN*x* heterojunction, supplying valid evidence of coupling between CN*x* and BOB. As depicted in Fig. 2c, Bi 4 f XPS spectra of BOB exhibited two typical peaks at 164.1 and 158.8 eV, which were ascribed to Bi 4 $f_{5/2}$ and Bi 4 $f_{7/2}$ of Bi^{3+}, respectively [21]. Once BOB combined with CN*x*, the binding energy (BE) of Bi^{3+} in 25BOB/CN*x* was negatively shifted around 0.1 eV, illustrating that the Bi species of BOB component in 25BOB/CN*x* hybrid acted as electron acceptor. Besides, two extra peaks appeared at 163.1 and 157.6 eV of lower BEs,

certifying the generation of Bi-N bonds [40]. An opposite phenomenon appeared in the N 1 s XPS spectra (Fig. 2d). For bare CN*x*, the peaks at 398.5, 400.6 and 404.2 eV corresponded to the C-N=C, N-(C)$_3$ and N-H$_x$, respectively [21]. The BEs of N involved components in 25BOB/CN*x* heterojunction positively shifted compared with those of pure CN*x*, demonstrating that the N elements of CN*x* component in 25BOB/CN*x* composite were the electron donor. Unlike Bi 4 f and N 1 s spectra, the peak positions of C 1 s (Fig. S3b), O 1 s (Fig. S3c) and Br 3d (Fig. S3d) barely changed after constructing heterojunction, inferring that electrons migrate between Bi and N species in 25BOB/CN*x* hybrid. The above results further confirmed that the interfacial chemical bond between CN*x* and BOB was linked via Bi-N bond.

Whereafter, the functional groups and chemical structures of samples were explored through FT-IR spectroscopy. Fig. 2e illustrated that the absorption band at 518 cm^{-1} for pristine BOB belonged to the Bi-O stretching [41,42]. For CN*x*, the absorption peaks situated at 1210–1634 cm^{-1} and 809 cm^{-1}, assigning to the C-N heterocycles and triazine units, respectively [42,43]. After coupling CN*x* with BOB, the stretching vibration of C-N heterocycles and Bi-O bonds coexist in the BOB/CN*x* composites. Particularly, a fresh peak emerged at about 1079 cm^{-1} (labeled with orange square lines) in all BOB/CN*x*

heterojunctions and the intensity of absorption peak significantly strengthened as the increasing of BOB, which could be originated from the Bi-N bond. The above phenomena could be obviously discovered in the enlarged area between 1050 and 1100 cm^{-1} (Fig. 2e). The aforementioned conclusion illustrated that a chemically bonded interface has been successfully built between BOB and CNx across Bi-N bonds, which was in accord with the simulated length of Bi-N (2.59 Å), as displayed in Fig. 2f. In addition, the defect sites of the as-prepared samples were detected by EPR spectra. As presented in Fig. 2g, almost no EPR signal occurred in the pristine BOB at about g = 2.004, inversely, a weak EPR signal appeared in the CN. After introducing defect into CN, the CNx presented high EPR signal, deducing that abundant N vacancies existed in CNx. Even though BOB mixed with CNx, the EPR intensities of mixed 25BOB/CNx and CNx were almost unchanged. A similar phenomenon appeared on 25BOB/CN without N defect. Unlike mixed 25BOB/CNx and 25BOB/CN, the EPR intensities of 25BOB/CNx slightly decreased compared to that of pure CNx, which could be attributed to the bonding effect among Bi and unsaturated N in CNx, reducing the number of unpaired electrons. Beyond that the corresponding quantitative analysis of defect sites was implemented and delineated in Fig. 2h.

To further reveal the coordination environment and electronic structure of 25BOB/CNx, X-ray absorption near-edge structure (XANES) and extended X-ray absorption fine structure (EXAFS) spectroscopy at Bi L2-edge were implemented. As illustrated in Fig. 3a, the absorption energy of 25BOB/CNx slightly shifted to a low-energy direction in contrast to pure BOB, revealing that the Bi ion presented decreased valence state in 25BOB/CNx heterojunction, which could probably be attributed to the replacement of O by low electronegative N at the heterojunction interface. Fourier transformed EXAFS spectra (Fig. 3b) of pristine BOB exhibited two main peaks at around 1.71 Å and 3.66 Å, corresponding to the first shell coordination of Bi−O and Bi−Bi bonds, respectively [44]. It is apparent that 25BOB/CNx presented an increased Bi−O bond intensity and a decreased bond length (0.04 Å) due to the formation of Bi−N bonds, along with the coordination number of Bi ion reducing. Subsequently, EXAFS fitting was performed to extract the structural parameters of Bi atoms (Fig. 3c). The obtained coordination

number of the center atom Bi was about 3.5 (Table S1), owing to the contribution N and O atoms. According to the k space of EXAFS as displayed in Fig. 3d and Fig. S4, the coordination environment of Bi in 25BOB/CNx heterojunction was different from that of pristine BOB. As observed from the wavelet transforms (WT) contour plots of BOB (Fig. 3e), the intensity maxima at 3.98 Å^{-1} and 5.85 Å^{-1} were assigned to the Bi−O and Bi−Bi contribution, respectively. The WT contour plot of 25BOB/CNx (Fig. 3f) presented one maximum intensity at 3.96 Å^{-1} and one at 5.81 Å^{-1}, which could be pertained to the Bi−O/N and Bi−Bi, respectively. These results indicated that BOB was firmly riveted on the CNx by the coordination with N atoms, as a result of stable heterostructure with strong interfacial interactions between BOB and CNx.

Whereafter, UV–vis diffuse reflectance spectroscopy (DRS) was measured to research photo-absorption ability of materials (Fig. S5). Compared to pristine CN, the absorption band edge of CNx apparently expanded to 467 from 441 nm, demonstrating that the existence of defects could availably extend the optical absorption. After introducing BOB, the light response properties of BOB/CNx hybrids were slightly lowered, however, it still had stronger absorption capacity than that of BOB. Little by little, the light absorption edges of BOB/CNx redshifted as the loading content of BOB reduced, which were more distinctly observed from the enlarged region between 400 and 450 nm (Fig. S6). In addition, 25BOB/CNx presented wider optical absorption tail than 25BOB/CN without N defects (Fig. S7), which further confirmed that the introduction of N vacancy was conducive to the expansion of light absorption.

In addition, the bandgap energy (E_g) of CN, CNx and BOB could be calculated on the basis of the function as follows: $\alpha h\nu = A(h\nu - E_g)^{n/2}$ [45]. The n values were determined to be 4 for CN, CNx and BOB due to their characters of indirect semiconductor [20,33]. Thus, the calculated E_g of CN, CNx and BOB were 2.61, 2.35 and 2.85 eV, respectively, which were presented in Fig. 4a. Accordingly, flat band potential (E_{fb}) of CN, CNx and BOB were explored by M−S plots (Fig. 4b). The E_{fb} values of CN, CNx and BOB were − 0.92, − 0.86 and − 0.42 V vs Ag/AgCl (−0.72, −0.66 and −0.22 V vs NHE), respectively [22,46]. Moreover, it could be found from M-S plots that all samples belonged to n-type
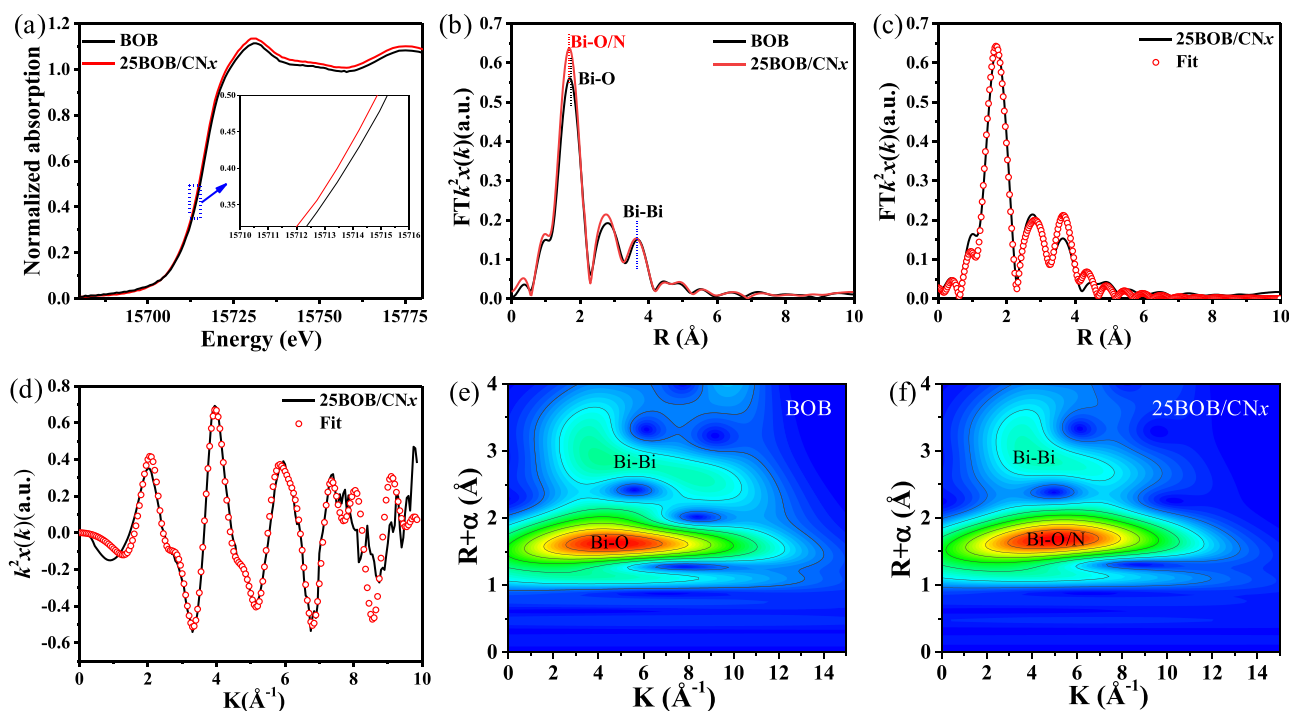

Fig. 3. (a) XANES spectra at the Bi L2-edge of pristine BOB and 25BOB/CNx; (b) k^2-weighted $\chi(k)$ function of the EXAFS spectra; (c) The EXAFS fitting for 25BOB/CNx; (d) EXAFS fitting curves of 25BOB/CNx at k space; Wavelet transform (WT) of (e) BOB and (f) 25BOB/CNx.
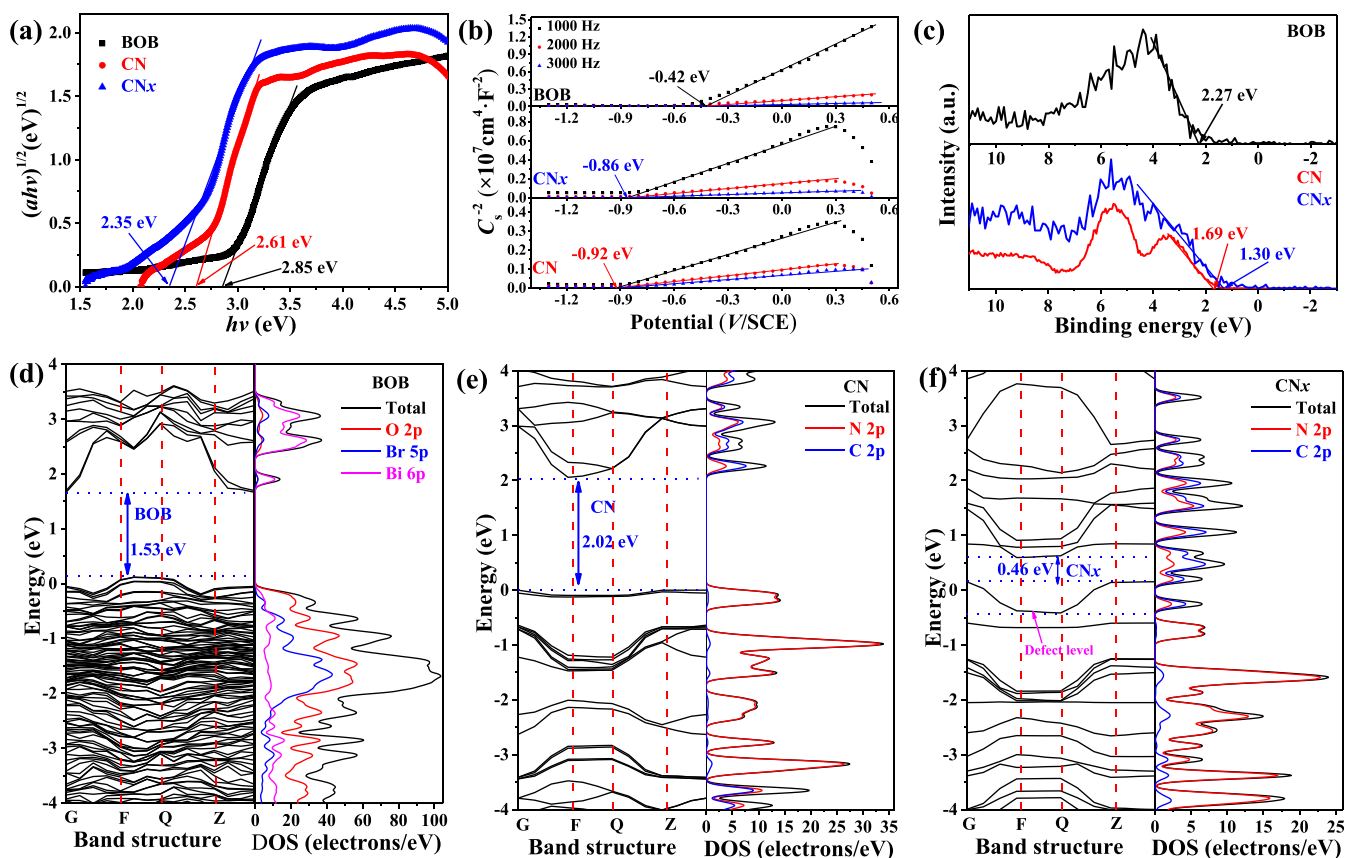
Fig. 4. (a) Tauc plots, (b) Mott−Schottky (M−S) curves, and (c) valence−band XPS (VB−XPS) spectra of BOB, CN and CN*x*; Calculated band structures and density of states (DOS) of (d) BOB, (e) CN and (f) CN*x*.

semiconductors due to their positive slopes. Subsequently, the E_{CB} of CN, CN*x* and BOB were − 0.82, − 0.76 and − 0.32 eV, respectively, since the E_{CB} value was 0.10 V more negative than E_{fb} for *n*-type semiconductor. According to formula $E_{VB} = E_{CB} + E_g$ [47,48], the corresponding E_{VB} of CN, CN*x* and BOB were measured to be 1.79, 1.59 and 2.53 eV, which have been attested through VB-XPS spectra (Fig. 4c). The E_{VB} of CN, CN*x* and BOB were 1.69, 1.30 and 2.27 eV from VB−XPS spectra, respectively, which trended towards those from M−S curves.

The DOS and band structures of CN, CN*x*, BOB and 25BOB/CN*x* were conducted by DFT calculations. It could be observed that calculated band gap was about 1.53 eV for BOB (Fig. 4d). Besides, the CB and VB was primarily contributed by Bi 6p state and O 2p orbital, respectively. For pure CN (Fig. 4e), the CB was basically consisted of C 2p orbital, while the VB was chiefly dominated by N 2p states. After introducing N defect (Fig. 4f), the contribution of orbitals was basically the same as those of CN, but a new defect level appeared in CN*x*, leading to the lower band gap. Once BOB combined with CN*x* (Fig. S8), the energy gap was lowered from 1.53 eV (BOB) to 1.49 eV (BOB/CN*x*), illustrating that the construction of heterojunction could expand the visible light absorption of BOB. As can be observed from the corresponding DOS, significant changes occur in the donor energy level, leading to an increased overlap of C and N 2p orbitals. Furthermore, the VB energy level of BOB/CN*x* was mainly contributed by O 2p and N 2p orbitals, while the CB energy level was hybridized by Bi 6p, O 2p and N 2p states, forming a strong hybrid orbital.

3.2. Photoredox activity and mechanism

The synergetic CO_2 photoconversion and TC oxidation in one reactive system was implemented to assess the photoredox activity of materials. For all the photocatalysts evaluated, CO was the main product

but H_2 and O_2 were not detected during the process of CO_2 photoreduction coupled with TC oxidation (Fig. S9). As displayed in Fig. 5a and b, a poor photoreduction performance of CO_2 appeared on pristine CN. After introducing N defects, the CO and CH_4 yields of CN*x* significantly increased with the extension of light time, illustrating that the formation of defects availably ameliorated the photocatalytic activity. Once BOB was introduced into CN*x*, which not only driven the reduction of CO_2, but also accelerated the decomposition of TC. Furthermore, as the deposition of BOB increasing, the photo-redox performance firstly heightened, attained the maximum at *n* = 25 wt%, and then declined (Fig. 5c). Besides, the apparent quantum yield (AQY) of 25BOB/CN*x* reached 1.02% under monochromatic light irradiation of 420 nm, which was 6.8 and 5.7 times of BOB (0.15%) and CN*x* (0.18%), respectively, indicating that the construction of heterojunction could availably enhance the quantum efficiency of 25BOB/CN*x* (Fig. S10). In addition, the action spectra (AQY as a function of wavelength) over 25BOB/CN*x* were recorded to probe the accurate visible range in which the modified samples were excited and reduced CO_2. Expectedly, the AQY values of 25BOB/CN*x* composite were plotted against wavelength, the data points fell well on the corresponding absorption spectrum (Fig. S11). Nevertheless, when BOB and CN*x* were mechanically mixed with a weight ratio of 25 wt% (marked as mixed 25BOB/CN*x*), the photo-redox activity clearly lowered (Fig. 5d and Figs. S12a and b). It further manifested that the interfacial Bi-N bonds was formed between BOB and CN*x*, thus resulting in the rapid migration and separation of photogenerated carriers, and further boosting photo-redox activity for CO_2 conversion and TC degradation. Except for interfacial chemical bonds, the introduced N vacancy could also directly affect the photocatalytic performance. Compared to 25BOB/CN heterojunction without N defects, the 25BOB/CN*x* photocatalyst delineated an excellent photoredox performance, illustrating that the N defects played a critical role
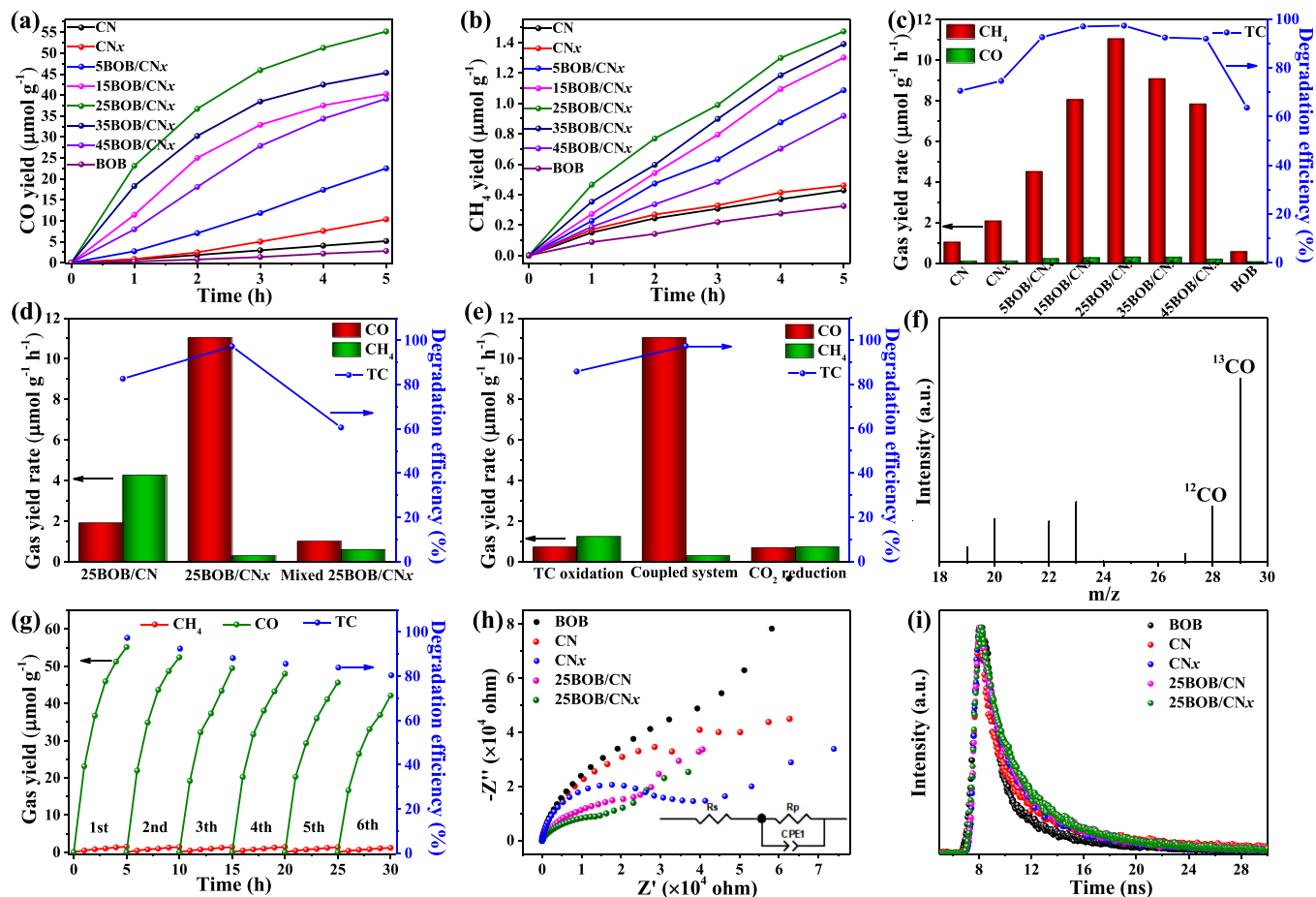
Fig. 5. Time-dependent production of (a) CO and (b) CH$_4$ for diverse times, and (c) gas yield rate and degradation efficiency of various samples; (d) Photoredox activity of 25BOB/CN without defect and mechanical mixed 25BOB/CN*x*; (e) Effect of diverse reaction systems on 25BOB/CN*x*; (f) Mass patterns of the gaseous products over 25BOB/CN*x* using isotope-labeled $^{13}CO_2$ as substrate; (g) Cycling runs of 25BOB/CN*x* for photo-redox coupling CO$_2$ conversion with TC degradation; (h) EIS curves and (i) time-resolved fluorescence decay curves of catalysts.

in supplying plentiful reactive sites and expediting the separation of carriers, thus enhancing the photocatalytic redox reaction. Whereafter, the 25BOB/CN*x* composite was served as a model photocatalyst in the following tests for further conference.

Take into consideration that the cooperative reaction system could make full use of photogenerated charges and then influence the photo-redox activity. Hence, the impact of diverse reaction systems on 25BOB/CN*x* was investigated. In comparison with two half-reactions, such designed dual-functional reaction system exhibited outstanding photocatalytic performance (Fig. 5e), and the relevant time courses of CH$_4$ and CO yield were presented in Figs. S13a and b. As previously mentioned, the establishment of coupling reaction systems was another key factor for improving photocatalytic performance. In addition, carbon sources were tracked by using $^{13}CO_2$ as reactant gas (Fig. 5f). Upon $^{13}CO_2$ replaced $^{12}CO_2$, not only the ^{13}CO peak was found, but also traces ^{12}CO was detected from mass spectra. Besides, the total organic carbon (TOC) value of TC mineralization over 25BOB/CN*x* in coupled reaction system was further examined, and the mineralization rate of TC attained 87.2%, indicating that vast majority of TC molecules had been broken down completely into CO$_2$ and H$_2$O. The above results further confirmed that most of the gas products stemmed from the injected CO$_2$, and tiny products came from CO$_2$ of TC mineralization.

In addition, the effects of diverse TC concentrations on the photo-catalytic performance for CO$_2$ reduction over 25BOB/CN*x* composite were investigated. Fig. S14a-c displayed that the productive rates of CO and CH$_4$ boosted steadily as the TC concentration increasing, until TC concentration reached 20 mg L^{-1}, and then lowered. The

aforementioned phenomena illustrated that although the inductive TC efficaciously expedited carrier separation, the introduction of superfluous TC overlay active sites on the surface of catalyst, bringing about insufficient contact between reactants and reactive sites. Considering that the solution pH may change surface charge property of catalyst and thus affect its adsorption and photocatalytic performance, the effect of solution pH values on the photocatalytic CO$_2$ reduction coupled with TC oxidation over 25BOB/CN*x* was explored (Fig. S15). It can be observed that 25BOB/CN*x* presented excellent photocatalytic redox activity in the pH range of 4.0–8.0, which covered the pH values of most wastewater. Nevertheless, extreme acidic (pH $\leq$ 2.0) or alkaline (pH $\geq$ 10.0) conditions were not conducive to the photocatalytic redox reaction. To explain the above phenomenon, Zeta potentials of 25BOB/CN*x* under the pH values from 2.0 to 10.0 were implemented. It can be seen from Fig. S16 that the point of zero charge (pH$_{PZC}$) of 25BOB/CN*x* was about 6.14. Since TC molecule could form cationic species (TCH$_3^+$), neutral species (TCH$_2^0$), and monoanionic species (TCH$_3^-$) under pH $<$ 3.3, 3.3 $<$ pH$<$ 7.7, and pH $>$ 7.7 conditions [49]. Thus, the electrostatic repulsion reduced the adsorption of TC on the 25BOB/CN*x* surface at pH = 2.0 and pH = 10.0, thereby leading to low photocatalytic redox performance.

Besides, colorless phenol and colored rhodamine B (RhB), as typical pollutants, were used to explore the effect of organic pollutants with different electron donating power on photocatalytic performance for CO$_2$ reduction. Figs. S17a-c depicted that the imported organic pollutants could effectively promote CO$_2$ photoreduction. Especially, when TC molecules were introduced, the photocatalytic performance of CO$_2$

conversion was greatly improved in comparison to the presence of phenol and RhB molecules. To understand the electron-donating ability of organic molecules on the BOB/CNx surface, the charge density difference of TC, RhB and phenol molecules on the BOB/CNx surface were calculated. As presented in Figs. S18a–c, the electron transfer number of TC on the BOB/CNx substrate (1.982 e) was larger than that of RhB (1.236 e) and phenol (0.591 e). The aforesaid verdict delineated that TC molecules possessed strong electron-donating ability for significantly enhancing the CO$_2$ photoreduction performance.

Ultimately, recycling tests were conducted to explored the durability of 25BOB/CNx heterojunction. It could be observed that the photocatalytic redox activity of 25BOB/CNx for synergetic TC decomposition and CO$_2$ conversion decreased by 16.9% and 13.4 μmol g^{-1}, respectively, after six continuous runs (Fig. 5g), which should be due to the loss of catalyst mass when collecting powders after each cycle. Moreover, XRD patterns, of 25BOB/CNx hybrid before and after reaction manifested that the phase structure was still well maintained (Fig. S19). In addition, SEM image (Fig. S20) and FT-IR spectra (Fig. S21) of 25BOB/CNx after 6 cycles were implemented. No evident change in morphology and chemical structure could be observed, which verified remarkable stability of 25BOB/CNx material during the TC degradation coupled with CO$_2$ reduction. Beyond that, the 25BOB/CNx presented superior photoreduction activity of CO$_2$ in the presence of TC than most reported materials [50–56], which have been summarized in Table S2. Despite the activity of CO$_2$ photoreduction for BiOI/g-C$_3$N$_4$ [57] was slightly superior to that for 25BOB/CNx in this work, it was either poor the selectivity or high catalyst dosage. Hence, the as-obtained 25BOB/CNx catalyst would make great improvement in quantum efficiency.

Soon afterwards, the transfer resistance of electrons has been proved by electrochemical impedance spectrum (EIS). As illustrated in Fig. 5h, among all samples, 25BOB/CNx heterojunction presented a smallest arc radius, verifying that the synergic action of defects and Bi-N bond would immensely advance the interfacial charge mobility in the 25BOB/CNx composite, thereby accelerating the separation and transfer of charges. To analyze the quantitative consequence, the fitted values of impedance were summarized in Table S3. And the homologous fitting equivalent circuit was embedded in Fig. 5h, in which the fitting R_s and R_p values were the ohmic resistance between electrode and sample, as well as the transfer resistance of charges in catalyst, respectively. It is quite clear that different catalysts owned approximate R_s values, inversely, presented enormous variations of R_p values. The corresponding R_p values of BOB, CN, CNx, 25BOB/CN and 25BOB/CNx samples were 68475, 62518, 61907, 16085 and 11098 Ω, respectively. Dramatically, the 25BOB/CNx had a smallest R_p values, which affirmed its low charge transfer resistance and fast charge transfer rate. Apparently, the BOB and CNx with low surface charge transfer efficiency (η_{CTE}) were around 23.7% and 25.7%, respectively (Fig. S22a and b). However, once coupling of them, the η_{CTE} of 25BOB/CNx was significantly increased to 68.3% (Fig. S22c), further proving that the synergistic effect of interfacial Bi-N bond and N vacancy could boost charge transfer rate of 25BOB/CNx S-scheme heterojunction. Furthermore, transient photocurrent (TPC) response, as a direct indicator for interfacial separation efficiency of carriers, was also carried out. As illustrated in Fig. S23, the 25BOB/CNx heterojunction presented obviously enhanced TPC response compared with 25BOB/CN, let alone the single BOB, CN and CNx. The above-mentioned conclusions testified that the synergistic effect of defect and Bi-N bond not only modulated charge transfer of S-scheme heterostructures, but also afforded affluent active sites for participating in CO$_2$ photoreduction cooperative TC oxidation.

To investigate the effects of interfacial Bi-N bond and defects on the migration dynamics of charges, photoluminescence (PL) spectra was employed. As presented in Fig. S24, a strong PL signal was observed on pristine CN, however, once introducing N vacancy, the PL intensity of CNx obviously lowered, certifying that the defect could effectively reduce the recombination of photon-generated charges. After the introduction of BOB, the PL signal of 25BOB/CNx was obviously weaker

than that of pure CNx, BOB and 25BOB/CN without N vacancy, illustrating that the synergic action of defects and interfacial Bi-N bonds greatly promoted the separation rate of charges. Soon afterwards, the time-resolved PL (TRPL) decay curves was implemented to further probe the decay lifetimes of carriers. And the relevant parameters were summarized in Table S4. As exhibited in Fig. 5i, the 25BOB/CNx presented much longer average lifespan than that of BOB, CNx and 25BOB/CN, illustrating that the higher speed transfer of photoinduced charges in the 25BOB/CNx hybrid owing to the elevated electron migration process from BOB to CNx via Bi-N bond.

Take into consideration that the microstructure directly affects the adsorption properties of photocatalysts, the specific surface areas of the materials were measured by N$_2$ adsorption-desorption isotherms. It can be observed from Fig. 6a that all materials with type IV isotherms verified the presence of mesopores, which were in keeping with the relevant distribution plots of pore size (Fig. S25). It could be observed form summarized Brunauer–Emmett–Teller (BET) surface area in Table S5. After N defect was introduced into CN, the BET surface area of CNx could increase from 14.94 m^2 g^{-1} to 17.18 m^2 g^{-1}. Despite BOB with small BET surface area (16.26 m^2 g^{-1}) loaded on the CNx surface, the BET surface area of 25BOB/CNx heterojunction was significantly increased by 8.04 m^2 g^{-1}. The larger specific surface area could supply ample reactive sites for cooperative CO$_2$ conversion and TC oxidization. To further verify the above result, the CO$_2$ adsorption isotherms (Fig. 6b) of the as-synthesized samples were recorded. Compared with the other samples, 25BOB/CNx showed strong CO$_2$ adsorption capacity, which was consistent with the results of the N$_2$ sorption isotherms. Furthermore, the adsorption energies (E_{ads}) of CO$_2$ and TC molecule of CN, CNx, BOB as well as BOB/CNx with different sides were probed through the DFT calculations (Fig. 6c and d). Whereafter, the E_{ads} of CO$_2$ for CN, CNx and BOB were -0.29, -0.54 and -0.38 eV, respectively (Fig. 6c). Obviously, the CNx presented a smaller E_{ads} value than CN and BOB, demonstrating that CNx presented higher adsorption ability for CO$_2$ than CN and BOB. What's more, the E_{ads} of CO$_2$ for BOB and CNx side of BOB/CNx were -0.72 and -0.97 eV, respectively, illustrating that CO$_2$ was more likely to adsorb on CNx side of BOB/CNx but not BOB side. Unlike CO$_2$ adsorption, TC molecules were more likely to attach to the BOB side rather than CNx side of BOB/CNx (Fig. 6d). In addition, compared with 25BOB/CN and mixed 25BOB/CNx (Fig. S26), the 25BOB/CNx heterojunction presented stronger adsorption energy of CO$_2$ and TC molecules, which was attributed to the synergistic effect of Bi-N bonds and defects. The aforesaid ultimateness testified that CO$_2$ conversion and TC oxidation were inclined to occur on the CNx and BOB side of BOB/CNx heterojunction, respectively.

To further determine the feasible intermediate species during the photocatalytic process, first, the intermediate species of reducing half-reactions in coupled reaction systems were investigated. As seen from in situ Fourier-transform infrared spectroscopy (FTIR) spectra (Fig. 7a), the absorption band from 2340 to 2360 cm^{-1} pertained to CO$_2$ asymmetrical stretching [58], which increased with illumination time bit by bit. Whereafter, the adsorbed CO$_2$ molecules could react with H$_2$O to produce the monodentate carbonates (m-CO$_3^{2-}$) at 1320, 1473 and 1507 cm^{-1}, bidentate carbonates (b-CO$_3^{2-}$) at 1340 and 1654 cm^{-1} as well as bicarbonate (HCO$_3^-$) at 1418, 1437 and 1456 cm^{-1} in reactive system [59]. Beyond that some peaks at 1361, 1558 and 1577 cm^{-1} have been also detected, belonging to –COOH bending vibration [58, 59]. Furthermore, the –COOH signal gradually boosted but no evident location change as the increase of illumination time, illustrating that –COOH as significant intermediate species could participate in CO$_2$ photoreduction into CO. As can be seen, the absorption peak at 1718 cm^{-1} originated from the typical stretching vibration of CO [60–63]. Therewith, Gibbs free energy of BOB/CNx was calculated to insight into the kinetic energy barrier of each step. As observed from Fig. 7b, the *CO$_2$ was easily hydrogenated to *COOH intermediates over BOB/CNx via an energy barrier of 0.73 eV. Nevertheless, this step over pristine CNx with a barrier of 1.05 eV need to be overcome, which has
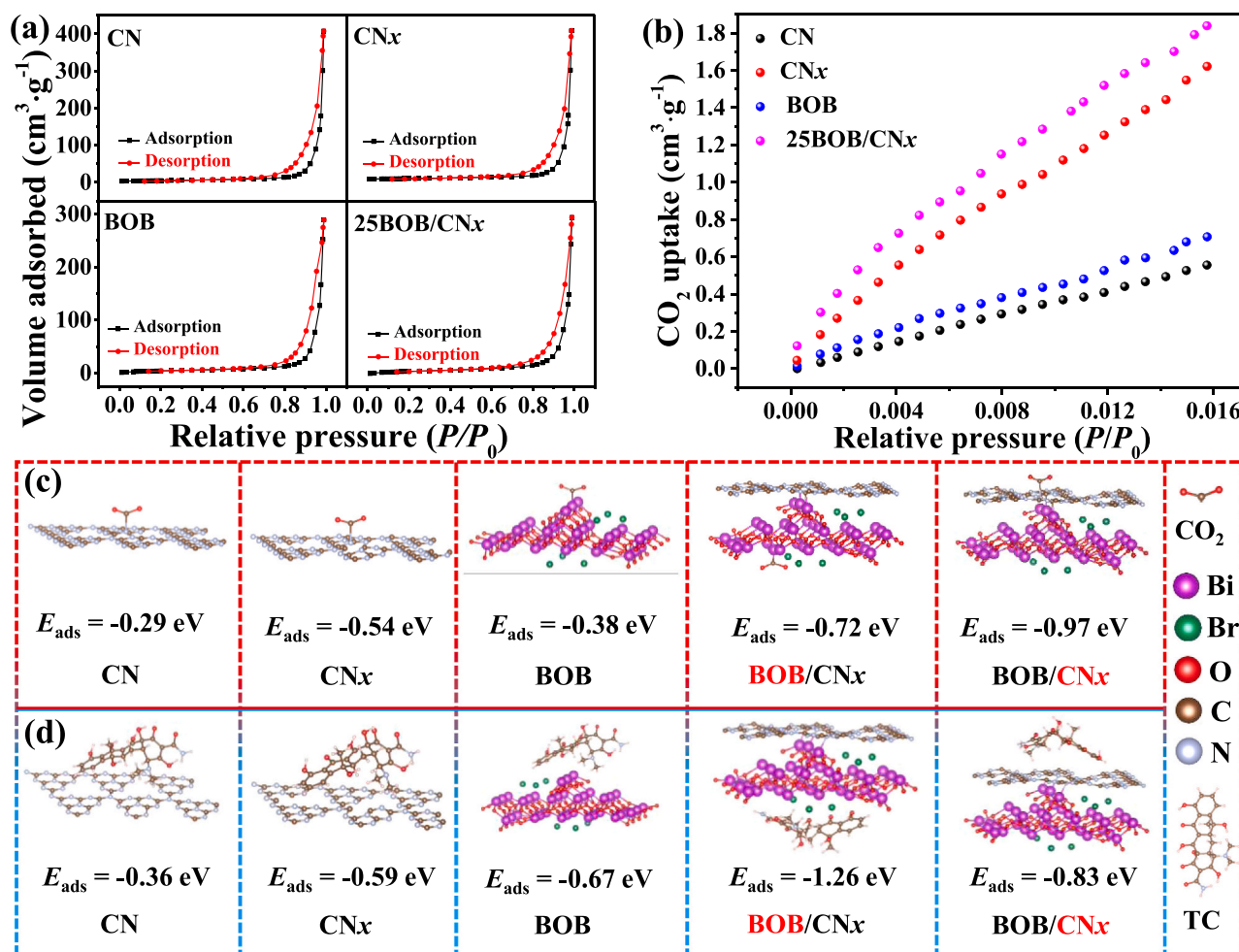
Fig. 6. (a) N_2 adsorption-desorption isotherms and (b) CO_2 adsorption isotherm of materials; The adsorption energies of (c) CO_2 and (d) TC molecules on CN, CNx, BOB, as well as BOB and CNx side of BOB/CNx.

been reported in our previous literature [20]. This further verified the excellent CO_2 activation ability of BOB/CNx. Soon afterwards, the *CO was formed by *COOH protonation process, which absorbed on the surface of catalyst. As it could be observed, the *CO was more liable to escape from BOB/CNx surface as ultimate product, rather than further reduced into *CHO, since the energy barrier of *CO was obviously lower than that of *CHO. The above phenomenon illustrated a great prospect for CO_2 reduction to CO over S-scheme BOB/CNx heterojunction, which was in good agreement with the different selectivity of product. And the relevant reaction route was provided in Fig. 7c. In the beginning, CO_2 molecules adsorbed on the surface of BOB/CNx (*CO_2) and then reacted with protons (H^+) and electrons (e^-) to generate the pivotal *COOH species. In quick succession, *COOH was further reduced into *CO adsorbed on the surface of BOB/CNx by capturing H^+ and e^-. Ultimately, CO escaped from BOB/CNx surface.

Whereafter, the intermediate products of TC decomposition were measured according to liquid chromograph-mass spectrometry (LC-MS) spectra (Fig. S27a-f). It can be seen from MS spectra that the primary intermediate products of TC mineralization were measured, whose m/z situated at 445, 461, 415, 410, 383, 360, 318, 299, 273, 171, 161, 154, 149, 127, and 111, belonging to various structures [64–66]. In quick succession, the reliable reaction pathway of TC oxidation was displayed in Fig. S28. Pathway I: The TC molecules firstly were attacked by •OH to generate intermediate P1 ($m/z = 461$). Whereafter, the P2 ($m/z = 415$) was formed by ring opening reaction of product P1, which farther produced the P3 ($m/z = 383$) by demethylations reaction. Then, P4 ($m/z = 318$) was generated by ring-opening, successive deamination

and dehydration. Pathway II: The TC molecule went through via loss of functional groups or ring-opening reaction to produce P6 ($m/z = 410$), and then farther dehydration for generation of P7 ($m/z = 360$). Subsequently, the P7 was converted to P8 ($m/z = 299$) and P9 ($m/z = 273$) through the open ring, deamination and dehydration. Finally, small molecular organic substances could be farther decomposed into small molecules, even could be absolutely oxidized into H_2O and CO_2.

3.3. The direction of electron migration

To further research the transfer direction of carriers at the interface of BOB/CNx hybrid, the ultraviolet photoelectron spectroscopy (UPS) was first explored using He I as excitation source. As exhibited in Fig. 8a-c, the cutoff energy (E_{cutoff}) of CN, CNx and BOB were 18.6, 18.7 and 17.9 eV, respectively, and the corresponding work function (Φ) were determined as 2.62, 2.52 and 3.32 V according to the formula $\Phi = h\nu - E_{cutoff}$ [67,68]. Furthermore, the work functions of CN, CNx and BOB were calculated through DFT calculations. As observed from Fig. 8d-f, the work functions of CN, CNx and BOB were 4.82, 4.72 and 5.02 eV, respectively. The BOB had higher Φ than CNx, which was basically consistent with the UPS result. The above results confirmed that the CNx had a low Fermi energy level (E_f) than CN, however, higher than BOB component before contact. Once CN and BOB came into contact, electrons tend to flow from CN to BOB, resulting in a decrease in the work function of BOB and an increase of CN (Fig. S29a). Eventually, an equilibrium is reached at 4.94 eV, where the potential difference across the interface disappears and the interface electric field, directed from CN
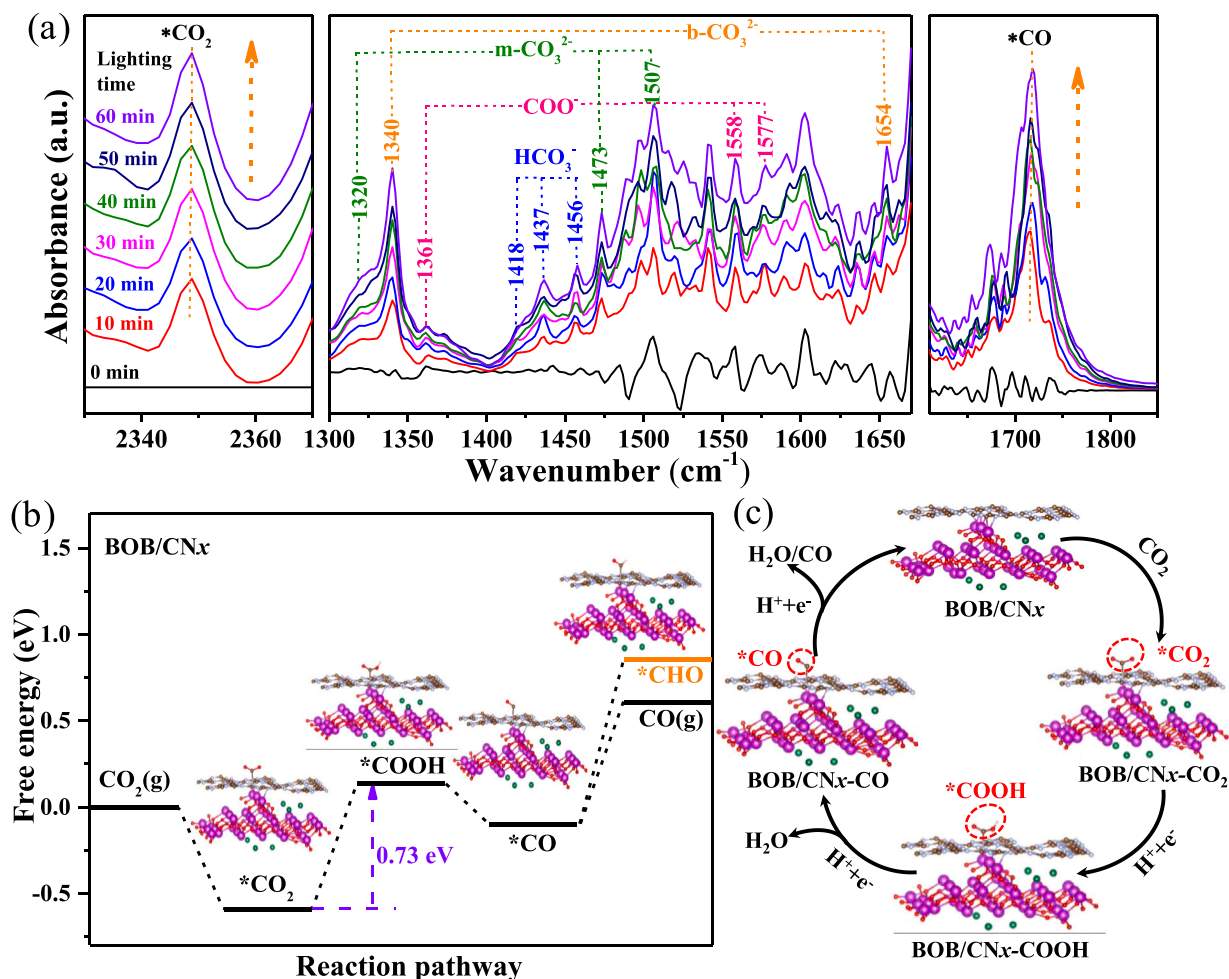
Fig. 7. (a) In situ FTIR spectra for CO_2 photoreduction over 25BOB/CN*x*; (b) Free energy diagrams of BOB/CN*x* for CO_2 conversion; (c) The feasible reaction route of CO_2 into CO over BOB/CN*x*.

to BOB, suppresses the excessive flow of electrons. A similar phenomenon occurred with the BOB/CN*x* heterojunction (Fig. S29b). As displayed in Fig. 8g, When CN*x* was intimately contacted with BOB in darkness, the electrons spontaneously migrated into BOB from CN*x* though the interface until their E_f attained equilibrium. Therewith, the negative and positive charges accumulated in the interface area adjacent BOB and CN*x*, respectively. Since the charge density in BOB component accumulated whereas in CN*x* component depleted, bringing about the downward and upward bending of band edges for BOB and CN*x*, respectively. In addition, the above mechanism of electron migration was further confirmed by the charge density difference of BOB/CN*x* heterojunction. As shown in Fig. 8h, the average planar charge density difference of BOB/CN*x* was negative on BOB and positive on CN*x* side, delineating that electrons transport from CN*x* to BOB through interface electric field. According to Bader charge analysis, about 0.967 e transfer from CN*x* to BOB (Fig. 8i).

To investigate the root of high photocatalytic performance of BOB/CN*x* heterojunction, the separation and transfer behaviors of charges were systematically tracked. First, in-situ irradiated XPS, as one of valid tools, was implemented to explore the migration direction of electrons. As delineated in Fig. 9a-b, once exposed to visible light, the BEs of Bi 4 f and N 1 s peaks in 25BOB/CN*x* heterojunction were positively and negatively shifted, respectively, compared with that in the absence of illumination. This illustrated the reduced electron density on the Bi species and the increased electron density on the N states. On the contrary, the BEs of C 1 s (Fig. 9c), O 1 s (Fig. S30a) and Br 3d (Fig. S30b) spectra in 25BOB/CN*x* hybrid barely changed before and after

illumination. This conclusion further manifested that the electron migrated from Bi sites of BOB to N species of CN*x* component in the 25BOB/CN*x* hybrid across the interfacial Bi-N chemical bond under the light irradiation, proving that carrier transfer path followed S-scheme migration mode. Subsequently, in situ Kelvin-probe force microscopy (KPFM), as a powerful technique, was conducted to directly visualize the transfer direction of charges in semiconductor. Fig. 9d and g displayed the height mapping images of 25BOB/CN*x* heterojunction with and without irradiation, respectively. As presented in Fig. 9e and h, the KPFM images of 25BOB/CN*x* changed obviously in the dark and light. And the homologous surface potential profiles were depicted in Fig. 9f and i. Compared with 25BOB/CN*x* before illumination, the surface potential of BOB point increased about 27 mV and CN*x* point reduced by 28 mV under light irradiation. The above results convincingly confirmed that the photoinduced electrons transferred from BOB to CN*x* through the interfacial chemical bond, leading to the accumulation of electrons on the surface of CN*x*. In other words, once BOB/CN*x* heterojunction was exposed to visible light, the photoelectrons would flow in the reverse orientation from BOB to CN*x*, leading to the formation of S-scheme transfer mode.

To furnish more evidences of the S-scheme migratory highway in BOB/CN*x* heterojunction, the dominating reaction species, such as superoxide radicals ($\bullet O_2^-$) and hydroxyl radicals ($\bullet OH$), were explored by ESR. It can be observed from Fig. S31 that $\bullet O_2^-$ and $\bullet OH$ signals could not be observed in darkness. Obviously, for simplex BOB, hardly any $\bullet O_2^-$ signal was found, nevertheless, the overt $\bullet OH$ signal was detected exposed to light, certifying that BOB could generate $\bullet OH$ rather than
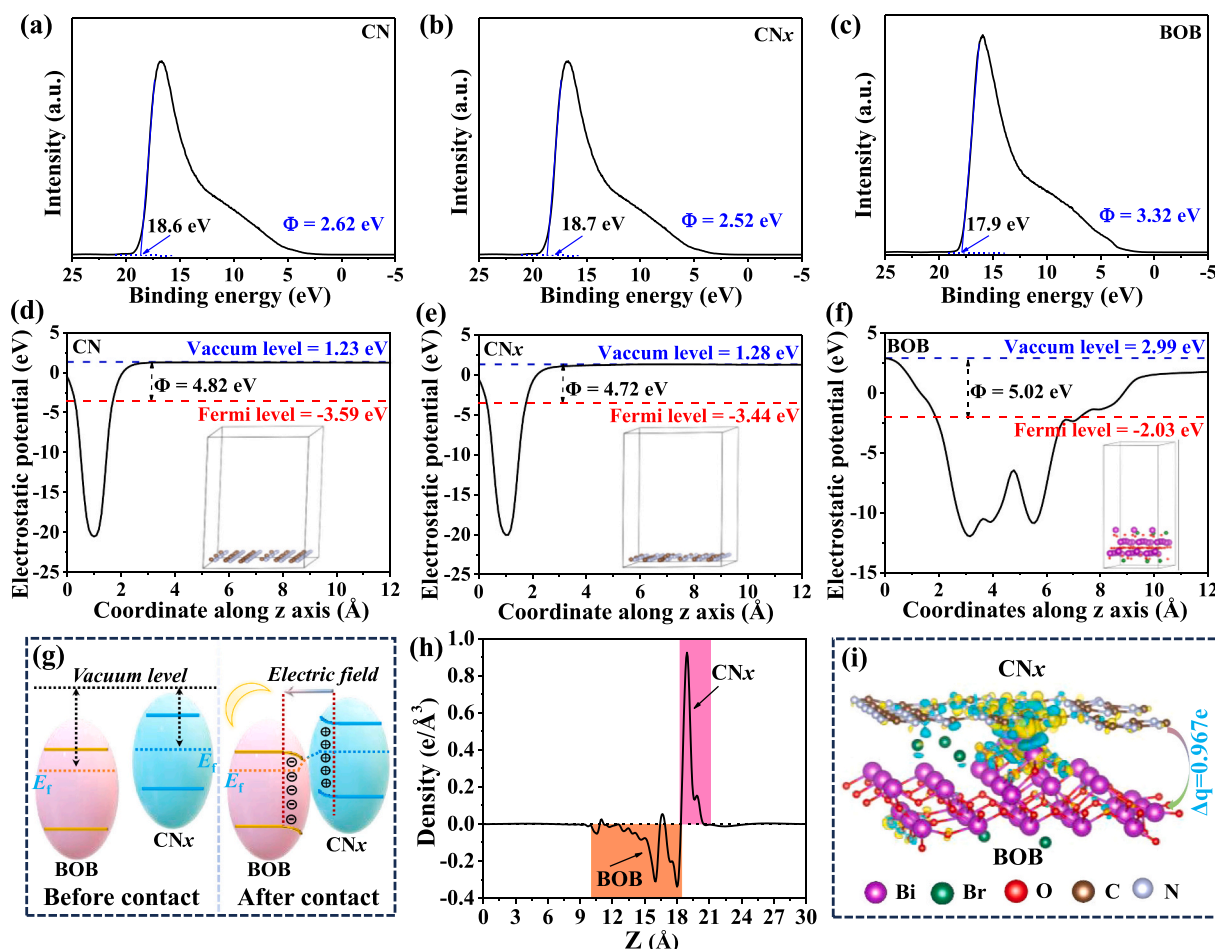
Fig. 8. UPS spectra of (a) CN (b) CN*x* and (c) BOB; Work functions of (d) CN, (e) CN*x* and (f) BOB; (g) Diagram of electron migration between BOB and CN*x* before and after contacted in the dark; (h) Average planar electron density difference $\Delta\rho(z)$ and (i) three-dimensional charge density difference of BOB/CN*x* heterojunction (the yellow and cyan regions represented charge accumulation and depletion, respectively.).

$\bullet O_2^-$. Inversely, the $\bullet$OH peak was hardly discovered but the $\bullet O_2^-$ peak was explicitly discovered in pristine CN*x*, illustrating that the CN*x* could form $\bullet O_2^-$ rather than $\bullet$OH. The aforementioned phenomena were principally ascribed to the fact that pure BOB possessed weaker reduction potential than $O_2/\bullet O_2^-$ (−0.33 V vs NHE) [49,69] but stronger oxidation potential than $OH^-/\bullet OH$ (1.99 V vs NHE) [70,71], on the contrary, the redox potential of CN*x* was higher than that of $O_2/\bullet O_2^-$ but lower than that of $OH^-/\bullet OH$. After combining BOB with CN*x*, the $\bullet$OH and $\bullet O_2^-$ signals of 25BOB/CN*x* heterojunction were higher than those of pristine BOB and CN*x*, verifying that the formation of BOB/CN*x* composite effectually accelerated the separation rate of photogenerated charges, thereby favoring the generation of active species.

To probe the reaction mechanism of the simultaneous CO_2 photoreduction and TC oxidation, capture experiments were performed by using isopropanol (IPA), benzoquinone (BQ), triethanolamine (TEOA) and $KBrO_3$ as the trapping agent of $\bullet$OH, $\bullet O_2^-$, h$^+$ and e$^-$, respectively [72–74]. As displayed in Fig. S32, after IPA and BQ addition, the photo-redox activity of 25BOB/CN*x* had hardly any noticeable change. Once $KBrO_3$ was introduced, the yields of gaseous products (CO and CH_4) were significantly reduced, but the TC degradation efficiency was almost unchanged. On the contrary, after the addition of TEOA, a distinct inhibitory activity for TC removal was noticed, but little significant change for CO_2 photoreduction. The above conclusions indicated that e$^-$ and h$^+$ were pivotal active species involved in photocatalytic synergistic reaction, which were used for CO_2 reduction and TC oxidation in coupled reaction systems, respectively.

Combined with aforesaid perorations, a conceivable mechanism over

BOB/CN*x* hybrid was put forward in Fig. 9j. Once photoexcitation, CN*x* and BOB could generate photoelectrons and holes. Therewith, the photoexcited electrons migrated via an S-scheme transfer pattern to drive photoreduction of CO_2 congenerous oxidative decomposition of TC. That is to say, the relatively bootless holes on VB of CN*x* could recombine with unnecessary electrons on CB of BOB through the Bi-N bond, simultaneously, the strong reducing capacity of electrons accumulated on CB of CN*x*, meanwhile, the high oxidizing capacity of holes were retained on VB of BOB. Soon afterwards, the highly reducing electrons could directly reduce CO_2 into CH_4 and CO, in the meantime, the strongly oxidizing holes would oxidize TC into CO_2 and H_2O, thus accomplishing the complete utilization of charges and high-efficiency photo-redox properties for TC mineralization and CO_2 reduction. This study further illustrated that the interfacial chemical bond and defects co-modulate charge transfer of S-scheme heterostructures with high-quality charge separation to came true the synergetic energy generation and environmental remediation.

4. Conclusions

In summary, a new-style BOB/CN*x* S-scheme junction with interfacial Bi-N bond and defect was fabricated and applied for congenerous CO_2 reduction and wastewater treatment. The interfacial Bi-N bond as electron bridge could expedite the migration and separation of charges, meanwhile, N defect was liable to not only expand light absorption, but also provide more active sites. Benefiting from the collaboratively improved migration rate of charges by interfacial Bi-N bond and N
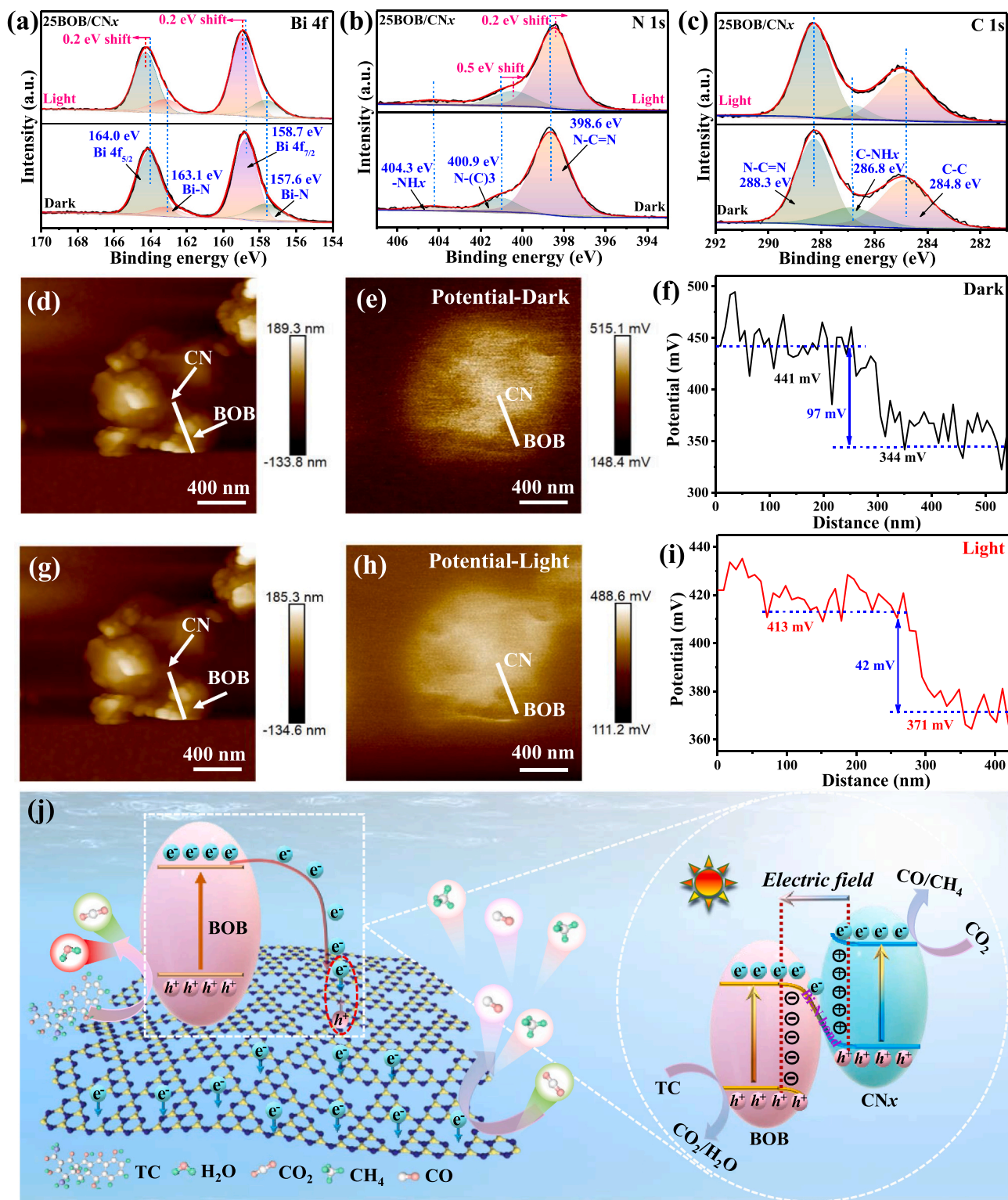
Fig. 9. In-situ XPS high-resolution spectra of (a) Bi 4 f, (b) N 1 s and (c) C 1 s of 25BOB/CN*x* heterojunction with and without illumination; (d, g) AFM topography, (e, h) KPFM image and (f, i) surface potential profiles of the 25BOB/CN*x* heterojunction in darkness (d, e, f) and in the light (g, h, i); (j) Photo-induced carriers transfer mechanism of BOB/CN*x* heterojunction under visible light illumination.

defect, the BOB/CN*x* could actualize outstanding photo-redox activity for CO$_2$ conversion integrated with TC removal. In addition, such designed coupling reaction system could effectively make full use of carriers, thus boosting the utilization rate of charges and the photo-redox performance. This study emphasized the pivotal role of interfacial Bi-N bond and defect in adjusting charge migration kinetics and

provided a doable pathway to establish S-scheme heterojunction for environmental remediation and renewable energy generation.

CRediT authorship contribution statement

Xuemei Jia: Funding acquisition, Formal analysis, Validation,

Writing – review & editing. **Jing Cao:** Funding acquisition, Formal analysis, Writing – review & editing. **Haoyu Sun:** Formal analysis, Validation, investigation, Resources. **Xinyue Li:** Formal analysis, Resources. **Haili Lin:** Funding acquisition, Validation. **Shifu Chen:** Funding acquisition, Supervision.

Declaration of Competing Interest

The authors declare that they have no known competing financial interests or personal relationships that could have appeared to influence the work reported in this paper.

Data Availability

Data will be made available on request.

Acknowledgements

Appendix A. Supporting information

Supplementary data associated with this article can be found in the online version at doi:10.1016/j.apcatb.2023.123522.

References

[1] H. Tong, S. Ouyang, Y. Bi, N. Umezawa, M. Oshikiri, J. Ye, Nano-photocatalytic materials: possibilities and challenges, Adv. Mater. 24 (2012) 229–251.

[2] X.N. Wang, F.L. Wang, Y.H. Sang, H. Liu, Full-spectrum solar-light-activated photocatalysts for light chemical energy conversion, Adv. Energy Mater. 7 (2017) 1700473.

[3] V. Hasija, A. Kumar, A. Sudhaik, P. Raizada, P. Singh, O.V. Le, T.T. Le, V. H. Nguyen, Step-scheme heterojunction photocatalysts for solar energy, water splitting, CO_2 conversion, and bacterial inactivation: a review, Environ. Chem. Lett. 19 (2021) 2941–2966.

[4] J. Zhang, Q. Bai, X. Bi, C. Zhang, M. Shi, W.W. Yu, F. Du, L. Wang, Z. Wang, Z. Zhu, N. Sui, Piezoelectric enhanced peroxidase-like activity of metal-free sulfur doped graphdiyne nanosheets for efficient water pollutant degradation and bacterial disinfection, Nano Today 43 (2022) 101429.

[5] B. Wang, C. Bozal-Ginesta, R. Zhang, B. Zhou, H. Ma, L. Jiao, L. Xu, E. Liu, C. Wang, Z. Li, A supramolecular $H_{12}SubPcB$-OPhCOPh/TiO_2 Z-scheme hybrid assembled via dimeric concave-ligand π-interaction for visible photocatalytic oxidation of tetracycline, Appl. Catal. B 298 (2021) 120550.

[6] X. Peng, J. Wu, Z. Zhao, X. Wang, H. Dai, Y. Wei, G. Xu, F. Hu, Activation of peroxymonosulfate by single atom Co-N-C catalysts for high-efficient removal of chloroquine phosphate via non-radical pathways: electron-transfer mechanism, Chem. Eng. J. 429 (2022) 132245.

[7] C. Li, H. Wu, D. Zhu, T. Zhou, M. Yan, G. Chen, J. Sun, G. Dai, F. Ge, H. Dong, High-efficient charge separation driven directionally by pyridine rings grafted on carbon nitride edge for boosting photocatalytic hydrogen evolution, Appl. Catal. B 297 (2021) 120433.

[8] L. Ran, Z.W. Li, B. Ran, J.Q. Cao, Y. Zhao, T. Shao, Y.R. Song, M.K.H. Leung, L. C. Sun, J.G. Hou, Engineering single-atom active sites on covalent organic frameworks for boosting CO_2 photoreduction, J. Am. Chem. Soc. 144 (2022) 17097–17109.

[9] H.N. Shi, H.Z. Wang, Y.C. Zhou, J.H. Li, P.L. Zhai, X.Y. Li, G.G. Gurzadyan, J. G. Hou, H. Yang, X.W. Guo, Atomically dispersed indium-copper dual-metal active sites promoting C–C coupling for CO_2 photoreduction to ethanol, Angew. Chem. Int. Ed. 61 (2022), e202208904.

[10] X.B. Chen, S.H. Shen, L.J. Guo, S.S. Mao, Semiconductor-based photocatalytic hydrogen generation, Chem. Rev. 110 (2010) 6503–6570.

[11] X.M. Zhang, P.L. Zhai, Y.X. Zhang, Y.Z. Wu, C. Wang, L. Ran, J.F. Gao, Z.W. Li, B. Zhang, Z.Z. Fan, L.C. Sun, J.G. Hou, Engineering single-atomic Ni-N_4-O sites on semiconductor photoanodes for high-performance photoelectrochemical water splitting, J. Am. Chem. Soc. 143 (2021) 20657–20669.

[12] L. Ran, S. Qiu, P.L. Zhai, Z.W. Li, J.F. Gao, X.M. Zhang, B. Zhang, C. Wang, L. C. Sun, J.G. Hou, Conformal macroporous inverse opal oxynitride-based photoanode for robust photoelectrochemical water splitting, J. Am. Chem. Soc. 143 (2021) 7402–7413.

[13] Y.R. Song, X.M. Zhang, Y.X. Zhang, P.L. Zhai, Z.W. Li, D.F. Jin, J.Q. Cao, C. Wang, B. Zhang, J.F. Gao, L.C. Sun, J.G. Hou, Engineering MoO_x/MXene hole transfer

[14] layers for unexpected boosting of photoelectrochemical water oxidation, Angew. Chem. Int. Ed. 61 (2022), e202200946.

[14] Y. Li, B.H. Li, D.L. Zhang, L. Cheng, Q.J. Xiang, Crystalline carbon nitride supported copper single atoms for photocatalytic CO_2 reduction with nearly 100% CO selectivity, ACS Nano 14 (2020) 10552–10561.

[15] Q.T. Han, X.W. Bai, Z.Q. Man, H.C. He, L. Li, J.Q. Hu, A. Alsaedi, T. Hayat, Z.T. Yu, W.H. Zhang, J.L. Wang, Y. Zhao, Z.G. Zou, Convincing synthesis of atomically thin, single crystalline $InVO_4$ sheets toward promoting highly selective and efficient solar conversion of CO_2 into CO, J. Am. Chem. Soc. 141 (2019) 4209–4213.

[16] K.Q. Lu, Y.H. Li, F. Zhang, M.Y. Qi, X. Chen, Z.R. Tang, Y.M.A. Yamada, M. Anpo, M. Conte, Y.J. Xu, Rationally designed transition metal hydroxide nanosheet arrays on graphene for artificial CO_2 reduction, Nat. Commun. 11 (2020) 5181.

[17] H. Huang, J. Zhao, Y. Du, C. Zhou, M. Zhang, Z. Wang, Y. Weng, J. Long, J. Hofkens, J.A. Steele, M.B.J. Roeffaers, Direct Z-scheme heterojunction of semicoherent $FAPbBr_3$/Bi_2WO_6 interface for photoredox reaction with large driving force, ACS Nano 14 (2020) 16689–16697.

[18] N. Luo, T. Montini, J. Zhang, P. Fornasiero, E. Fonda, T. Hou, W. Nie, J. Lu, J. Liu, M. Heggen, L. Lin, C. Ma, M. Wang, F. Fan, S. Jin, F. Wang, Visible-light-driven coproduction of diesel precursors and hydrogen from lignocellulose-derived methylfurans, Nat. Energy 4 (2019) 575–584.

[19] Q. Guo, F. Liang, X.B. Li, Y.J. Gao, M.Y. Huang, Y. Wang, S.G. Xia, X.Y. Gao, Q. C. Gan, Z.S. Lin, C.H. Tung, L.Z. Wu, Efficient and selective CO_2 reduction integrated with organic synthesis by solar energy, Chem 5 (2019) 2605–2616.

[20] X.M. Jia, C. Hu, H.Y. Sun, J. Cao, H.L. Lin, X.Y. Li, S.F. Chen, A dual defect co-modified S-scheme heterojunction for boosting photocatalytic CO_2 reduction coupled with tetracycline oxidation, Appl. Catal. B 324 (2023), 122232.

[21] C. Hu, J. Cao, X.M. Jia, H.Y. Sun, H.L. Lin, S.F. Chen, Difunctional Ni_2P decorated novel Z-scheme $BiVO_4$/g-C_3N_4 heterojunction for achieving highly efficient CO_2 reduction and tetracycline oxidation, Appl. Catal. B 337 (2023), 122957.

[22] X.M. Jia, H.Y. Sun, H.L. Lin, J. Cao, C. Hu, S.F. Chen, In-depth insight into the mechanism on photocatalytic selective CO_2 reduction coupled with tetracycline oxidation over $BiO_{1-x}Br$/g-C_3N_4, Appl. Surf. Sci. 614 (2023), 156017.

[23] G. Xu, H. Zhang, J. Wei, H.X. Zhang, X. Wu, Y. Li, C. Li, J. Zhang, J. Ye, Integrating the g-C_3N_4 nanosheet with B-H bonding decorated metal-organic framework for CO_2 activation and photoreduction, ACS Nano 12 (2018) 5333–5340.

[24] D. Liang, J.C. Wu, C. Xie, J. Wen, Y.H. Lyu, Z. Sofer, J.Y. Zheng, S.Y. Wang, Efficiently and selectively photocatalytic cleavage of C–C bond by C_3N_4 nanosheets: defect-enhanced engineering and rational reaction route, Appl. Catal. B 317 (2022) 121690.

[25] H. Yu, R. Shi, Y. Zhao, T. Bian, Y. Zhao, C. Zhou, G.I.N. Waterhouse, L.Z. Wu, C. H. Tung, T. Zhang, Alkali-assisted synthesis of nitrogen deficient graphitic carbon nitride with tunable band structures for efficient visible-light-driven hydrogen evolution, Adv. Mater. 29 (2017) 1605148.

[26] D. Ruan, S. Kim, M. Fujitsuka, T. Majima, Defects rich g-C_3N_4 with mesoporous structure for efficient photocatalytic H_2 production under visible light irradiation, Appl. Catal. B 238 (2018) 638–646.

[27] C.V. Krishnan, B.S. Brunschwig, C. Creutz, N. Sutin, Homogeneous catalysis of the photoreduction of water. 6. Mediation by polypyridine complexes of ruthenium(II) and cobalt(II) in alkaline media, J. Am. Chem. Soc. 107 (1985) 2005–2015.

[28] H. Tada, T. Mitsui, T. Kiyonaga, T. Akita, K. Tanaka, All-solid-state Z-scheme in CdS–Au–TiO_2 three-component nanojunction system, Nat. Mater. 5 (2006) 782–786.

[29] Q.L. Xu, L.Y. Zhang, B. Cheng, J.J. Fan, J.G. Yu, S-scheme heterojunction photocatalyst, Chem 6 (2020) 1543–1559.

[30] X.F. Li, J.F. Zhang, Z.L. Wang, J.W. Fu, S.M. Li, K. Dai, M. Liu, Interfacial C-S bonds of g-C_3N_4/$Bi_19Br_3S_{27}$ S-scheme heterojunction for enhanced photocatalytic CO_2 reduction, Chem. Eur. J. 29 (2023), e202202669.

[31] Y. Zhang, J. Di, X.W. Zhu, M.X. Ji, C. Chen, Y.N. Liu, L.N. Li, T.G. Wei, H.M. Li, J. X. Xia, Chemical bonding interface in $Bi_2Sn_2O_7$/BiOBr S-scheme heterojunction triggering efficient N_2 photofixation, Appl. Catal. B 323 (2023), 122148.

[32] Y.Y. Yang, C.G. Niu, D.W. Huang, H. Guo, H.P. Feng, L. Li, H.Y. Liu, Q.Q. Fan, M. Z. Qin, Appropriate oxygen vacancies and Mo-N bond synergistically modulate charge transfer dynamics of MoO_{3-x}/S-CN for superior photocatalytic disinfection: Unveiling synergistic effects and disinfection mechanism, J. Hazard. Mater. 445 (2023), 130481.

[33] W.D. Zhang, X.L. Liu, X.A. Dong, F. Dong, Y.X. Zhang, Facile synthesis of $Bi_{12}O_{17}Br_2$ and $Bi_4O_5Br_2$ nanosheets: In situ DRIFTS investigation of photocatalytic NO oxidation conversion pathway, Chin. J. Catal. 38 (2017) 2030–2038.

[34] K.Y. Gao, C.M. Zhang, Y. Zhang, X.Y. Zhou, S. Gu, K.H. Zhang, X.F. Wang, X. J. Song, Oxygen vacancy engineering of novel ultrathin $Bi_{12}O_{17}Br_2$ nanosheets for boosting photocatalytic N_2 reduction, J. Colloid Interface Sci. 614 (2022) 12–23.

[35] F. Wang, N. Ma, L. Zheng, L. Zhang, Z.Y. Bian, H. Wang, Interface engineering of p-p Z-scheme BiOBr/$Bi_{12}O_{17}Br_2$ for sulfamethoxazole photocatalytic degradation, Chemosphere 307 (2022) 135666.

[36] D.Q. Zeng, W.J. Ong, H.F. Zheng, M.D. Wu, Y.Z. Chen, D.L. Peng, M.Y. Han, $Ni_{12}P_5$ nanoparticles embedded into porous g-C_3N_4 nanosheets as a noble-metal-free hetero-structure photocatalyst for efficient H_2 production under visible light, J. Mater. Chem. A 5 (2017) 16171–16178.

[37] J. Ma, C. Wang, H. He, Enhanced photocatalytic oxidation of NO over g-C_3N_4-TiO_2 under UV and visible light, Appl. Catal. B 184 (2016) 28–34.

[38] J. Gong, Z.Y. Zhang, Z.P. Zeng, W.J. Wang, L.X. Kong, J.Y. Liu, P. Chen, Graphene quantum dots assisted exfoliation of atomically-thin 2D materials and as-formed 0D/2D van der Waals heterojunction for HER, Carbon 184 (2021) 554–561.

[39] Q.F. Han, J.W. Pang, X. Wang, X.D. Wu, J.W. Zhu, Synthesis of unique flowerlike Bi_2O_2 (OH)(NO_3) hierarchical microstructures with high surface area and superior photocatalytic performance, Chem. Eur. J. 23 (2017) 3891–3897.

[40] G.S. Zhou, Y.R. Xu, Y. Cheng, Z.H. Yu, B.H. Wei, X.L. Liu, Z.R. Chen, C.X. Li, Z. Y. Lu, Rapid dissociation of high concentration excitons between $[Bi_2O_2]^{2+}$ slabs with multifunctional N-Bi-O sites for selective photoconversion into CO, Appl. Catal. B 335 (2023), 122892.

[41] L.Q. Ye, J.Y. Liu, Z. Jiang, T.Y. Peng, L. Zan, Facets coupling of BiOBr-g-C_3N_4 composite photocatalyst for enhanced visible-light-driven photocatalytic activity, Appl. Catal. B 142–143 (2013) 1–7.

[42] X.N. Hu, Y. Zhang, B.J. Wang, H.J. Li, W.B. Dong, Novel g-C_3N_4/$BiOCl_xI_{1-x}$ nanosheets with rich oxygen vacancies for enhanced photocatalytic degradation of organic contaminants under visible and simulated solar light, Appl. Catal. B 256 (2019), 117789.

[43] M.M. Zhang, C. Lai, B.S. Li, D.L. Huang, G.M. Zeng, P. Xu, L. Qin, S.Y. Liu, X.G. Liu, H. Yi, M.F. Li, C.C. Chu, Z. Chen, Rational design 2D/2D BiOBr/CDs/g-C_3N_4 Z-scheme heterojunction photocatalyst with carbon dots as solid-state electron mediators for enhanced visible and NIR photocatalytic activity: Kinetics, intermediates, and mechanism insight, J. Catal. 369 (2019) 469–481.

[44] J. Di, P. Song, C. Zhu, C. Chen, J. Xiong, M.L. Duan, R. Long, W.Q. Zhou, M.Z. Xu, L.X. Kang, B. Lin, D.B. Liu, S.M. Chen, C.T. Liu, H.M. Li, Y.L. Zhao, S.Z. Li, Q.Y. Yan, L. Song, Z. Liu, Strain-engineering of $Bi_{12}O_{17}Br_2$ nanotubes for boosting photocatalytic CO_2 reduction, ACS Mater. Lett. 2 (2020) 1025–1032.

[45] H.W. Huang, Y. He, X.W. Li, M. Li, C. Zeng, F. Dong, X. Du, T.R. Zhang, Y.H. Zhang, $Bi_2O_2(OH)(NO_3)$ as a desirable $[Bi_2O_2]^{2+}$ layered photocatalyst: strong intrinsic polarity, rational band structure and {001} active facets co-beneficial for robust photooxidation capability, J. Mater. Chem. A 3 (2015) 24547–24556.

[46] H.P. Feng, J.F. Yu, L. Tang, J.J. Wang, H.R. Dong, T. Ni, J. Tang, W.W. Tang, X. Zhu, C. Liang, Improved hydrogen evolution activity of layered double hydroxide by optimizing the electronic structure, Appl. Catal. B 297 (2021), 120478.

[47] A.Y. Shi, H.H. Li, S. Yin, J.C. Zhang, Y.H. Wang, H_2 evolution over g-C_3N_4/Cs_xWO_3 under NIR light, Appl. Catal. B 228 (2018) 75–86.

[48] Q.X. Liu, L.H. Ai, J. Jiang, MXene-derived $TiO_2@C$/g-C_3N_4 heterojunctions for highly efficient nitrogen photofixation, J. Mater. Chem. A 6 (2018) 4102–4110.

[49] X.M. Jia, Q.F. Han, H.Z. Liu, S.Z. Li, H.P. Bi, A dual strategy to construct flowerlike Z-scheme BiOBr/$BiOAc_{1-x}Br_x$ heterojunction with enhanced visible-light photocatalytic activity, Chem. Eng. J. 399 (2020) 125701.

[50] L. Wang, R.J. Chen, Z.Q. Zhang, X.R. Chen, J. Ding, J.F. Zhang, H. Wan, G.F. Guan, Constructing direct Z-scheme heterojunction g-C_3N_5/BiOBr for efficient photocatalytic CO_2 reduction with H_2O, J. Environ. Chem. Eng. 11 (2023), 109345.

[51] Y. Bai, T. Chen, P.Q. Wang, L. Wang, L.Q. Ye, X. Shia, W. Bai, Size-dependent role of gold in g-C_3N_4/BiOBr/Au system for photocatalytic CO_2 reduction and dye degradation, Sol. Energy Mater. Sol. Cells 157 (2016) 406–414.

[52] X. Jin, C. Lv, X. Zhou, H. Xie, S. Sun, Y. Liu, Q. Meng, G. Chen, A bismuth rich hollow $Bi_4O_5Br_2$ photocatalyst enables dramatic CO_2 reduction activity, Nano Energy 64 (2019), 103955.

[53] X.Y. Kong, B.J. Ng, K.H. Tan, X.F. Chen, H.T. Wang, A.R. Mohamed, S.P. Chai, Simultaneous generation of oxygen vacancies on ultrathin BiOBr nanosheets during visible-light-driven CO_2 photoreduction evoked superior activity and long-term stability, Catal. Today 314 (2018) 20–27.

[54] D.S. Li, B.C. Zhu, Z.T. Sun, Q.Q. Liu, L.L. Wang, H. Tang, Construction of UiO-66/ $Bi_4O_5Br_2$ Type-II heterojunction to boost charge transfer for promoting photocatalytic CO_2 reduction performance, Front. Chem. 9 (2021), 804204.

[55] Y. Bai, L.Q. Ye, T. Chen, P.Q. Wang, L. Wang, X. Shi, P.K. Wong, Synthesis of hierarchical bismuth-rich $Bi_4O_5Br_xI_{2-x}$ solid solutions for enhanced photocatalytic activities of CO_2 conversion and Cr(VI) reduction under visible light, Appl. Catal. B 203 (2017) 633–640.

[56] L. Ye, D. Wu, K.H. Chu, B. Wang, H. Xie, H.Y. Yip, P.K. Wong, Phosphorylation of g-C_3N_4 for photocatalytic CO_2 reduction, Chem. Eng. J. 304 (2016) 376–383.

[57] J.C. Wang, H.C. Yao, Z.Y. Fan, L. Zhang, J.S. Wang, S.Q. Zang, Z.J. Li, Indirect Z-scheme BiOI/g-C_3N_4 photocatalysts with enhanced photoreduction CO_2 activity under visible light irradiation, ACS Appl. Mater. Interfaces 8 (2016) 3765–3775.

[58] B. Wang, W. Zhang, G.P. Liu, H.L. Chen, Y.X. Weng, H.M. Li, P.K. Chu, J.X. Xia, Excited electron-rich $Bi^{(3-x)+}$ sites: a quantum well-like structure for highly promoted selective photocatalytic CO_2 reduction performance, Adv. Funct. Mater. 32 (2022) 2202885.

[59] J. Di, C. Chen, C. Zhu, R. Long, H.L. Chen, X.Z. Cao, J. Xiong, Y.X. Weng, L. Song, S. Z. Li, H.M. Li, Y.J. Xiong, Z. Liu, Surface local polarization induced by bismuth-oxygen vacancy pairs tuning non-covalent interaction for CO_2 photoreduction, Adv. Energy Mater. 11 (2021) 2102389.

[60] L.J. Liu, Y.Q. Jiang, H.L. Zhao, J.T. Chen, J.L. Cheng, K.S. Yang, Y. Li, Engineering coexposed 001 and 101 facets in oxygen-deficient TiO_2 nanocrystals for enhanced CO_2 photoreduction under visible light, ACS Catal. 6 (2016) 1097–1108.

[61] H. Zhao, L. Liu, J.M. Andino, Y. Li, Bicrystalline TiO_2 with controllable anatase-brookite phase content for enhanced CO_2 photoreduction to fuels, J. Mater. Chem. A 1 (2013) 8209–8216.

[62] S.W. Cao, Y. Li, B.C. Zhu, M. Jaroniec, J.G. Yu, Facet effect of Pd cocatalyst on photocatalytic CO_2 reduction over g-C_3N_4, J. Catal. 349 (2017) 208–217.

[63] S.Q. Gong, Y.L. Niu, X. Teng, X. Liu, M.Z. Xu, C. Xu, T.J. Meyer, Z.F. Chen, Visible light-driven, selective CO_2 reduction in water by In-doped Mo_2C based on defect engineering, Appl. Catal. B 310 (2022), 121333.

[64] Z. Li, C. Guo, J. Lu, Z. Hu, M. Ge, Tetracycline degradation by persulfate activated with magnetic $Cu/CuFe_2O_4$ composite: Efficiency, stability, mechanism and degradation pathway, J. Hazard. Mater. 373 (2019) 85–96.

[65] D. Huang, Q. Zhang, C. Zhang, R. Wang, R. Deng, H. Luo, T. Li, J. Li, S. Chen, C. Liu, Mn doped magnetic biochar as persulfate activator for the degradation of tetracycline, Chem. Eng. J. 391 (2020), 123532.

[66] H. Li, H.D. Ji, J.J. Liu, W. Liu, F. Li, Z.R. Shen, Interfacial modulation of $ZnIn_2S_4$ with high active Zr-S_4 sites for boosting photocatalytic activation of oxygen and degradation of emerging contaminant, Appl. Catal. B 328 (2023), 122481.

[67] X.H. Wang, X.H. Wang, J.F. Huang, S.X. Li, A. Meng, Z.J. Li, Interfacial chemical bond and internal electric field modulated Z-scheme S_v-$ZnIn_2S_4$/$MoSe_2$ photocatalyst for efficient hydrogen evolution, Nat. Commun. 12 (2021) 4112.

[68] X.Q. Zheng, L.P. Feng, Y.W. Dou, H.T. Guo, Y.C. Liang, G.Q. Li, J.J. He, P.F. Liu, J. He, High carrier separation efficiency in morphology-controlled BiOBr/C Schottky junctions for photocatalytic overall water splitting, ACS Nano 15 (2021) 13209–13219.

[69] M. Tang, Y. Ao, C. Wang, P. Wang, Rationally constructing a novel dual Z-scheme composite photocatalyst with significantly enhanced performance for neonicotinoid degradation under visible light irradiation, Appl. Catal. B 270 (2020), 118918.

[70] M. Tang, Y. Ao, C. Wang, P. Wang, Facile synthesis of dual Z-scheme g-C_3N_4/ Ag_3PO_4/AgI composite photocatalysts with enhanced performance for the degradation of a typical neonicotinoid pesticide, Appl. Catal. B 268 (2020), 118395.

[71] X. Peng, C. Liu, Z. Zhao, F. Hu, H. Dai, Construction of a Z-scheme g-C_3N_4/NBGO/ $BiVO_4$ heterostructure with visible-light driven photocatalytic degradation of tetracycline: efficiency, reaction pathway and mechanism, Catal. Sci. Technol. 12 (2022) 1339–1358.

[72] H.P. Feng, J.F. Yu, J. Tang, L. Tang, Y.N. Liu, Y. Lu, J.J. Wang, T. Ni, Y.Y. Yang, Y. Y. Yi, Enhanced electro-oxidation performance of FeCoLDH to organic pollutants using hydrophilic structure, J. Hazard. Mater. 430 (2022), 128464.

[73] Y.Y. Yang, H.P. Feng, C.G. Niu, D.W. Huang, H. Guo, C. Liang, H.Y. Liu, S. Chen, N. Tang, L. Li, Constructing a plasma-based Schottky heterojunction for near-infrared-driven photothermal synergistic water disinfection: synergetic effects and antibacterial mechanisms, Chem. Eng. J. 426 (2021), 131902.

[74] Y.Y. Yang, X.G. Zhang, C.G. Niu, H.P. Feng, P.Z. Qin, H. Guo, C. Liang, L. Zhang, H. Y. Liu, L. Li, Dual-channel charges transfer strategy with synergetic effect of Z-scheme heterojunction and LSPR effect for enhanced quasi-full-spectrum photocatalytic bacterial inactivation: new insight into interfacial charge transfer and molecular oxygen activation, Appl. Catal. B 264 (2020), 118465.